

1                   **Exact Bayesian Gaussian Cox Processes Using Random Integrals\***

2                   Bingjing Tang<sup>†</sup> and Julia Palacios<sup>‡</sup>

3

4       **Abstract.** The Gaussian Cox process is a popular model for point process data, in which the intensity function is a  
5       transformation of a Gaussian process. Posterior inference of this intensity function involves an intractable  
6       integral (i.e., the cumulative intensity function) in the likelihood resulting in doubly intractable posterior  
7       distribution. Here, we propose a nonparametric Bayesian approach for estimating the intensity function  
8       of an inhomogeneous Poisson process without reliance on large data augmentation or approximations of  
9       the likelihood function. We propose to jointly model the intensity and the cumulative intensity function,  
10      allowing us to directly bypass the need of approximating the cumulative intensity function in the likelihood.  
11      In this sense, our model is exact. We propose an MCMC sampler for posterior inference, test its performance  
12      on simulated data, and show that our method outperforms other exact and approximate methods. Finally,  
13      we demonstrate the utility of our method in three real-world scenarios including temporal and spatial event  
14      data, as well as aggregated time count data collected at multiple resolutions.

15       **Key words.** doubly intractable, Gaussian Cox processes, random integral, aggregated count data

16       **MSC codes.** 62G05, 62M20, 62M30

17       **1. Introduction.** Inhomogeneous Poisson process plays a fundamental role in modeling both  
18      temporal and spatial data with a variety of applications in many scientific fields [22]. Over the  
19      past decades, several approaches for inference have been proposed, including kernel smoothing  
20      methods [40, 14], reproducing kernel Hilbert space (RKHS)–based methods [7, 19], spline-based  
21      approaches [33, 10], and Bayesian frameworks [15, 2]. The classical nonparametric approach is  
22      the kernel smoothing estimator [14], which is closely related to kernel density estimation and offers  
23      computational simplicity and efficiency. In this work, our focus is on Bayesian inference of Gaussian  
24      Cox processes in which the intensity function is, a priori, modeled as a transformed Gaussian  
25      process.

26       Cox processes [11, 20], provide useful tools for modeling point process phenomena in a variety  
27      of fields of science and engineering including biology [26], astronomy [25], and many others [9]. It  
28      has been proved that many other classes of point processes such as the Gamma renewal process  
29      and the Weibull process are particular types of Cox processes [54]. Cox processes are also known as  
30      doubly stochastic Poisson processes, arising from inhomogeneous Poisson processes with a random  
31      intensity measure, which is in turn a realization from a second random process. In particular, in  
32      the context of Bayesian inference of the intensity function of an inhomogeneous process in which  
33      the intensity is, a priori, modeled as a transformed Gaussian process, the model is called Gaussian  
34      Cox process.

35       An important class of Gaussian Cox processes is the log Gaussian Cox processes [32], in which  
36      the log intensity function is a Gaussian process ensuring positivity of the intensity function. When  
37      covariates are available, the intensity of this model  $\lambda(x)$  is formulated as  $\lambda(x) = \exp\{X(t)\beta + g(s)\}$ ,  
38      a transformation of a linear combination of covariates  $X(t)\beta$  and Gaussian process  $g(s)$ . In this  
39      work, we will consider the no-covariates case. This transformed Gaussian process is a convenient  
40      flexible nonparametric prior model of the intensity function without restricting it to a particular  
41      functional form. Though the class of log Gaussian Cox processes possesses abundant appealing  
42      properties and it is widely used as a model for temporal and spatio-temporal point process data [15],  
43      the corresponding posterior inference of the intensity function is doubly intractable due to the  
44      intractability of the cumulative intensity function (the integral of the intensity function over data

---

\* Submitted to the editors 11/21/2024.

Funding: This work was supported in part by the NSF Career award 2143242 and NIH R35 GM14833801.

<sup>†</sup>Department of Statistics, Stanford University ([bingjing@stanford.edu](mailto:bingjing@stanford.edu)).

<sup>‡</sup>Department of Statistics, Stanford University ([juliapr@stanford.edu](mailto:juliapr@stanford.edu)).

45 domain) in the likelihood ( Equation (2.1)) [31, 37]. Therefore, inference methods either involve  
46 approximations in the likelihood or rely on computationally expensive data augmentation.

47 A classical approach assumes the intensity function is a finite-dimensional piecewise constant  
48 log-Gaussian function [32, 41, 43, 49, 51]. Bayesian inference of the intensity function is then  
49 performed by MCMC [29, 32, 41, 47, 48, 51], variational Bayes [51, 52], or integrated nested Laplace  
50 approximation (INLA) [43, 49]. While Variational Bayes is often the method of choice in Machine  
51 Learning, these methods have shown to be less computationally efficient than INLA [51, 52]. Among  
52 the three computational approaches, MCMC brings the most accuracy while INLA usually leads  
53 to fastest computation [49, 51]. An important aspect in the discretization methods is that the  
54 choice of change points (grids) controls the trade-off between numerical accuracy and computational  
55 efficiency [44].

56 Apart from those discretization methods, nonparametric Bayesian approaches have been pro-  
57 posed for exact MCMC or variational inference for Cox processes [2, 23, 24, 44]. Here ‘exact’ means  
58 all terms in the likelihood can be computed without approximations. [2] eliminates the need for  
59 approximating the cumulative intensity function by estimating an augmented posterior distribution  
60 of the intensity function and latent points via MCMC. Specifically, stimulated by the thinning algo-  
61 rithm of [27], a point-process variant of rejection sampling, [2] introduced latent (thinned) points in  
62 such a way that the joint distribution of observed and latent points follows a homogeneous Poisson  
63 process. Therefore the joint posterior inference of the intensity function and latent points could be  
64 easily implemented via standard MCMC samplers, e.g., a block Gibbs sampler. Since this approach  
65 does not involve any approximation error in the likelihood, its performance is more accurate than  
66 competing discretization methods. However, it has several limitations. First, its complexity is  
67 cubic in the number of all data points including both observed and latent points. Moreover, it is  
68 not applicable to high-dimensional input data since the expected number of latent points grows  
69 proportionally with the volume of the data domain. For instance, an  $n$ -dimensional hypercube with  
70 sides of length  $s$  has volume  $s^n$ .

71 Variational Bayesian approximations for Gaussian Cox processes have been recently proposed [3,  
72 16, 28]. These methods employ inducing points to reduce computation costs, albeit usually yielding  
73 less precise outcomes compared to the aforementioned exact MCMC inference approaches. [16]  
74 target an augmented posterior in which in addition to introducing thinning points (as in [2]), the  
75 authors add Pólya-Gamma marks to those points. This allows them to derive analytical expressions  
76 of variational posterior mean and covariance. However, their results depend on finite dimensional  
77 integrals which cannot be computed analytically. In [28], the authors restrict the intensity function  
78 to a quadratic function of a Gaussian process.

79 An alternative approach is to treat the cumulative intensity function as a latent random vari-  
80 able. [23] and [24] factor the intensity function as the product of the normalized intensity function  
81 and the cumulative intensity function, each with independent priors. The authors then place a Beta  
82 Dirichlet process mixture prior on the normalized intensity function, and a Jeffreys prior on the  
83 cumulative intensity function. Though this model is appealing theoretically, its MCMC posterior  
84 computation requires truncating the number of mixture components to a finite value, as is typically  
85 done in Dirichlet process mixture models. Similarly, [44] treats the cumulative intensity function  
86 as a latent variable with a Gamma prior, however the authors estimate the posterior distribution of  
87 the intensity function only at inducing points via MCMC. Motivated by improving scalability, the  
88 authors select the set of inducing points by optimizing an utility function in a similar fashion as [39].  
89 Instead of placing a functional prior on the intensity function, they construct a finite-dimensional  
90 prior on intensity function values at inducing and observed points together with the cumulative  
91 intensity function.

92 In this paper, in addition to placing a transformed Gaussian process prior on the intensity  
93 function, we a priori model the cumulative intensity function as a latent random variable. We then  
94 perform MCMC inference on the augmented posterior distribution of intensity function values at

95 observed and predicted locations together with the cumulative intensity function. Our proposed  
 96 method involves neither discretization nor heavy data augmentation. In this sense, our method  
 97 is exact as the likelihood is not approximated. Quite different from [23] and [44], though we also  
 98 conceive the cumulative intensity function as random, we employ a transformed Gaussian process  
 99 as the functional prior, which fortunately implies an analytical joint prior over the cumulative  
 100 intensity function and intensity function values at a finite set of locations. Moreover, we will show  
 101 that our proposed method can handle mixed data of recurrent events and binned counts, a prevalent  
 102 situation in applications in biology, ecology and survival analysis. To our knowledge, our method is  
 103 the first exact Gaussian Cox Processes method that infers intensity function from recurrent event  
 104 data, count data, and a mixture of both types. In particular, handling count data can be very  
 105 useful for analyzing large event datasets by grouping events into bins. In Section 2 we describe  
 106 the inferential problem and our proposed methods. In Section 3 we test the performance of our  
 107 method and compare it to state-of-art methods. We then demonstrate the utility of our method  
 108 in three real-world scenarios including temporal and spatial event data, as well as aggregated time  
 109 count data collected at multiple resolutions. Finally, we discuss extensions of our proposed method  
 110 to other point processes. Code implementation of our methods and documentation are available at  
 111 <https://github.com/exgpcp/RI>.

112 **2. Methods.** We assume two possible data scenarios. One in which we observe a set of  $N$   
 113 recurrent events  $\{s_n\}_{n=1}^N \in \mathcal{S}$ , and one in which we allow data to come as a mixture of recurrent  
 114 events  $\{s_n\}_{n=1}^N \in B_0 \subset \mathcal{S}$  and binned count data  $\{c_j\}_{j=1}^J$  that records the number of observed  
 115 events in  $\{B_j\}_{j=1}^J$ . Here  $\{B_j\}_{j=0}^J$  is a partition of  $\mathcal{S}$ . In both cases, we assume they are realizations  
 116 from an inhomogeneous Poisson process on  $\mathcal{S} \subset \mathbb{R}^D$  with intensity function  $\lambda(\cdot) : \mathcal{S} \rightarrow \mathbb{R}^+$ . In the  
 117 first case, the likelihood is

$$118 \quad (2.1) \quad p(\{s_n\}_{n=1}^N | \lambda) = \exp\{-\Lambda(\mathcal{S})\} \prod_{n=1}^N \lambda(s_n),$$

119 where  $\Lambda(\mathcal{S}) = \int_{\mathcal{S}} \lambda(s) ds$ , and in the second case, the likelihood is

$$120 \quad (2.2) \quad p(\{s_n\}_{n=1}^N, \{c_j\}_{j=1}^J | \lambda) = \exp\{-\Lambda(\mathcal{S})\} \prod_{n=1}^N \lambda(s_n) \prod_{j=1}^J \frac{\Lambda(B_j)^{c_j}}{c_j!}.$$

121 Typically,  $\lambda(s)$  is a priori modeled as a transformed Gaussian process. A Gaussian process is a  
 122 stochastic process such that function values at every finite set of locations follow a multivariate  
 123 Gaussian distribution [53]. The transformation is chosen to ensure  $\lambda(s) > 0 \forall s \in \mathcal{S}$ . Popular  
 124 choices for transformations are exponential [32] and sigmoid [2]. An important consequence of this  
 125 nonparametric prior is that  $\lambda(s)$  is a nonlinear transformation of a Gaussian process that is not  
 126 analytically tractable for integration and so the cumulative intensity functions  $\Lambda(\mathcal{S})$  and  $\{\Lambda(B_j)\}_{j=1}^J$   
 127 in Equations (2.1) and (2.2) become intractable. Moreover, the distribution of  $\Lambda(\mathcal{S})$  is not available  
 128 in closed form. To avoid this problem, we use an alternative transformation and a priori model  
 129  $\lambda(s)$ , at a finite set of points, and  $\Lambda(\mathcal{S})$  jointly. Similarly for the setting of Equation (2.2), we a  
 130 priori jointly model  $[\lambda(x_1), \dots, \lambda(x_M), \{\Lambda(B_j)\}_{j=0}^J]'$ . Before we define our prior, we will review  
 131 some properties of Gaussian processes in the next section.

132 **2.1. Unconstrained Gaussian processes.** It is a well known fact in the literature that if the  
 133 function  $f(x)$  is an unconstrained Gaussian process on  $\mathcal{X}$ ,  $\int_{\mathcal{X}} f(x) dx$  is a Gaussian functional  
 134 [21, 45, 53]. If  $\mathcal{X}$  is a fixed set, then  $\int_{\mathcal{X}} f(x) dx$  is a Gaussian random variable and the joint  
 135 vector of the Gaussian process evaluated at a finite set of locations and  $\int_{\mathcal{X}} f(x) dx$  is a multivariate  
 136 Gaussian vector. We present the detailed statement in Theorem 2.1 and its proof can be found in  
 137 Appendix A.

138     **Theorem 2.1.** Suppose the Gaussian process  $f(\cdot)$  on the compact space  $\mathcal{X}$  satisfies the assumption  
 139 that its mean function  $\mu(\cdot)$  and covariance kernel  $k(\cdot, \cdot)$  are integrable, i.e.,  $\int_{\mathcal{X}} \mu(s) ds$ ,  $\int_{\mathcal{X}} k(s, t) dt$   
 140 and  $\int \int_{\mathcal{X} \times \mathcal{X}} k(s, t) ds dt$  exist. For every finite set of vectors  $s_1, \dots, s_p \in \mathcal{X}$ , the vector  $\mathbf{f} :=$   
 141  $[f(s_1), \dots, f(s_p), \int_{\mathcal{X}} f(s) ds]'$  follows a Gaussian distribution and

$$142 \quad \mathbf{f} \sim \mathcal{N}\left(\boldsymbol{\mu}, \begin{pmatrix} \mathbf{V}_{SS} & \mathbf{V}_{SI} \\ \mathbf{V}'_{SI} & \mathbf{V}_{II} \end{pmatrix}\right),$$

143 where  $\boldsymbol{\mu} := [\mu(s_1), \dots, \mu(s_p), \int_{\mathcal{X}} \mu(s) ds]', \mathbf{V}_{SS}$  is the  $p \times p$  kernel matrix containing covariance  
 144 terms for all pairs of function values  $\{f(s_i)\}_{i=1}^p$ ,  $\mathbf{V}_{SI}$  is a  $p$ -dimensional vector formed by covariance  
 145 terms between function values  $\{f(s_i)\}_{i=1}^p$  and  $\int_{\mathcal{X}} f(s) ds$  with  $i$ -th term being  $\int_{\mathcal{X}} k(s_i, t) dt$ , and  $\mathbf{V}_{II}$   
 146 is the covariance of  $\int_{\mathcal{X}} f(s) ds$ , whose value is  $\int \int_{\mathcal{X} \times \mathcal{X}} k(s, t) ds dt$ .

147     Theorem 2.1 can be extended for a Gaussian process evaluated at any finite set of locations  
 148 and integrals over subsets of  $\mathcal{X}$ . That is, for subsets  $\{\mathcal{X}_i\}_{i=1}^q$  where  $\mathcal{X}_i \subset \mathcal{X}$ , the vector  $\mathbf{e} :=$   
 149  $[f(s_1), \dots, f(s_p), \int_{\mathcal{X}_1} f(s) ds, \dots, \int_{\mathcal{X}_q} f(s) ds]'$  follows a Gaussian distribution

$$150 \quad \mathbf{e} \sim \mathcal{N}\left(\tilde{\boldsymbol{\mu}}, \begin{pmatrix} \tilde{\mathbf{V}}_{SS} & \tilde{\mathbf{V}}_{SI} \\ \tilde{\mathbf{V}}'_{SI} & \tilde{\mathbf{V}}_{II} \end{pmatrix}\right),$$

151 where  $\boldsymbol{\mu} := [\mu(s_1), \dots, \mu(s_p), \int_{\mathcal{X}_1} \mu(s) ds, \int_{\mathcal{X}_q} \mu(s) ds]', \tilde{\mathbf{V}}_{SI}$  is a  $p \times q$  matrix formed by covariance  
 152 terms between function values  $\{f(s_i)\}_{i=1}^p$  and integral values  $\{\int_{\mathcal{X}_j} f(s) ds\}_{j=1}^q$  with  $ij$ -th term being  
 153  $\int_{\mathcal{X}_j} k(s_i, t) dt$ , and  $\tilde{\mathbf{V}}_{II}$  is a  $q \times q$  matrix containing covariance terms for all pairs of integral values  
 154  $\{\int_{\mathcal{X}_j} f(s) ds\}_{j=1}^q$  with  $ij$ -th term being  $\int \int_{\mathcal{X}_i \times \mathcal{X}_j} k(s, t) ds dt$ .

155     **2.2. Positive Gaussian prior.** For simplicity, we will focus on the setting in Equation (2.1)  
 156 and aim to define a joint prior on  $\boldsymbol{\lambda} := [\lambda(x_1), \dots, \lambda(x_M), \Lambda(\mathcal{S})]'$  at locations of interest, which  
 157 include both observed points  $\{s_n\}_{n=1}^N$ , and prediction (test) locations  $\{t_l\}_{l=1}^{M-N}$ , that is,  $\{x_i\}_{i=1}^M :=$   
 158  $\{t_l\}_{l=1}^{M-N} \cup \{s_n\}_{n=1}^N$ . Unfortunately, there is no equivalent Theorem 2.1 for truncated positive Gauss-  
 159 ian distributions. Generally, a linear function of truncated Gaussians is not truncated Gaussian, and  
 160 if  $[f(s_1), \dots, f(s_p)]'$  follows a truncated positive Gaussian distribution,  $[f(s_1), \dots, f(s_p), \int_{\mathcal{X}} f(s) ds]'$   
 161 neither follows a truncated multivariate Gaussian distribution nor has a nice analytic form of dis-  
 162 tribution. However, we can first specify an (unrestricted) Gaussian vector  $\mathbf{f}$  using Theorem 2.1,  
 163 and then define  $\boldsymbol{\lambda} = \mathbf{f} \cdot \mathbb{1}(\mathbf{f} > \mathbf{0})$ , imposing an additional positive constraint to  $\mathbf{f}$ . To be precise,  $\boldsymbol{\lambda}$   
 164 is a truncated positive Gaussian vector, i.e.,  $\boldsymbol{\lambda} \sim \mathcal{T}\mathcal{N}(\boldsymbol{\mu}, \mathbf{V})$ , with density:

$$165 \quad (2.3) \quad p(\boldsymbol{\lambda}) = \frac{\exp\left\{-\frac{1}{2}(\boldsymbol{\lambda} - \boldsymbol{\mu})' \mathbf{V}^{-1} (\boldsymbol{\lambda} - \boldsymbol{\mu})\right\}}{\int_{\mathcal{F}} \exp\left\{-\frac{1}{2}(\boldsymbol{\lambda} - \boldsymbol{\mu})' \mathbf{V}^{-1} (\boldsymbol{\lambda} - \boldsymbol{\mu})\right\} d\boldsymbol{\lambda}} \cdot \mathbb{1}(\boldsymbol{\lambda} > \mathbf{0})$$

166 where  $\mathcal{F} = \otimes_{i=1}^{M+1} [0, +\infty)$  and  $\mathbb{1}(\boldsymbol{\lambda} > \mathbf{0})$  is an indicator function that takes 1 if all elements of  $\boldsymbol{\lambda}$   
 167 are positive. In this work, we set mean  $\boldsymbol{\mu}$  to be zero, and define  $\mathbf{V}$  according to Theorem 2.1,  
 168 and the following two covariance kernels: the squared exponential kernel with hyperparameters  
 169  $\theta = (\theta_0, \theta_1)$ , i.e.,  $k_{SE}(x, x') = \theta_0 \exp\left(-\frac{\theta_1 \|x-x'\|^2}{2}\right)$ , and the Brownian motion covariance kernel  
 170 with a hyperparameter  $\theta$  denoting the precision parameter, i.e.,  $k_{BM}(x, x') = \frac{1}{\theta} \min(x, x')$  (see  
 171 their integrals in Appendix C). We also assume  $\mathcal{S} = [0, T]$  and  $T$  is known. In general, one can  
 172 select covariance kernels with analytic integrals, such as linear, squared exponential, and Brownian  
 173 motion covariance kernels [53]. To explore the expressive power of this positive prior, we simulate  
 174 100 samples and compare them to those from log-Gaussian and sigmoid-Gaussian processes, as  
 175 shown in Figure 10.

176        **2.2.1. Prior defined on observed and predicted locations.** The marginal prior on observed lo-  
 177        cations induced by [Equation \(2.3\)](#) is not a truncated Gaussian. We could have specified our prior on  
 178         $\boldsymbol{\lambda}_N := [\lambda(s_1), \dots, \lambda(s_N), \Lambda(\mathcal{S})]'$  only on observed points as in [Equation \(2.3\)](#). However, it is usually  
 179        of interest to sample from the predictive posterior distribution at unobserved points. One could ob-  
 180        tain the predictive distribution by defining a joint posterior on  $\boldsymbol{\lambda}$ , on both observed and unobserved  
 181        locations, and integrating out the posterior over intensity function values (and cumulative intensi-  
 182        ties) at observed locations and hyperparameters. For this, we would need to define a joint prior on  
 183         $\boldsymbol{\lambda}$ , normally via  $q(\boldsymbol{\lambda}) = q(\lambda(t_1), \dots, \lambda(t_{M-N}) | \boldsymbol{\lambda}_N)p(\boldsymbol{\lambda}_N)$ , where  $q(\lambda(t_1), \dots, \lambda(t_{M-N}) | \boldsymbol{\lambda}_N)$  can  
 184        be conveniently defined as a truncated Gaussian. However,  $q(\boldsymbol{\lambda}) \neq p(\boldsymbol{\lambda})$  (with  $p(\cdot)$  as defined in  
 185        [Equation \(2.3\)](#)). Moreover, simulating from  $q(\lambda(t_1), \dots, \lambda(t_{M-N}) | \boldsymbol{\lambda}_N)$  (i.e., truncated Gaussian)  
 186        is often time consuming. Instead, we picked  $p(\boldsymbol{\lambda})$  as our prior. Although this distribution is also  
 187        truncated Gaussian, we will later show that we actually do not need to sample from this prior  
 188        directly. For our posterior inference, using the  $p(\cdot)$  prior results in a posterior that is easier to  
 189        sample from than using the  $q(\cdot)$  prior. We conveniently define the joint prior with prediction points  
 190        as it is all that is needed for posterior inference.

191        A nuisance in the definition of the induced marginal prior on observed locations is that its  
 192        definition changes as we change the prediction set. This is not the case for Gaussian priors as  
 193        marginals remain in the same family. One potential concern would be the posterior sensitivity to  
 194        the choice of prediction set when the number of observed locations is small. In our experiments, we  
 195        observe that the induced marginal prior exhibits asymptotic convergence as described in [Appendix B](#), implying that the induced marginal prior on observed locations becomes effectively stable  
 196        as the size of the prediction set exceeds some threshold  $N$ . For example, in one-dimensional space,  
 197         $N \approx 20$  as suggested by our experiment results. When the size of users' selected prediction is very  
 198        small, to avoid the sensitivity, we suggest that users add additional locations to the prediction set,  
 199        for example, in one-dimensional space, we suggest at least 20 prediction points.

201        **2.3. Posterior inference.** We are interested in estimating the posterior

202        (2.4)        
$$p(\boldsymbol{\lambda}, \theta | \{x_i\}_{i=1}^M) \propto p_\theta(\theta) \cdot \mathcal{T}\mathcal{N}(\boldsymbol{\lambda}; \mathbf{0}, V_\theta) \cdot \exp\{-\Lambda(\mathcal{S})\} \cdot \prod_{n=1}^N \lambda(s_n),$$

203        where the covariance  $V_\theta$  is constructed from the kernel function  $k_\theta(\cdot, \cdot)$  as described in [Theorem 2.1](#),  
 204        and the mean of the GP prior is assumed to be zero. For the Brownian Motion covariance kernel, we  
 205        estimate the posterior distribution via Metropolis-within-Gibbs sampling in two steps, alternating  
 206        between  $\boldsymbol{\lambda}$  and  $\theta$ . For the squared exponential kernel we take an empirical Bayes approach : we  
 207        estimate the hyperparameter  $\theta$  from the data, then plug the estimate into the prior before doing  
 208        Bayesian inference.

209        **To sample from the full conditional**

210        (2.5)        
$$p(\boldsymbol{\lambda} | \theta, \{x_i\}_{i=1}^M) \propto \mathcal{N}(\boldsymbol{\lambda}; \mathbf{0}, V_\theta) \mathbb{1}(\Lambda(\mathcal{S}) > 0) \exp\{-\Lambda(\mathcal{S})\} \prod_{i=1}^M \mathbb{1}(\lambda(x_i) > 0) \prod_{n=1}^N \lambda(s_n).$$

211        via a Metropolis-Hastings algorithm with Gaussian proposal would lead to rare acceptance due to  
 212        the positivity constraint. A Metropolis-Hastings algorithm with truncated Gaussian proposals such  
 213        as the one proposed in [29] would lead to both inefficiency in sampling from truncated multivariate  
 214        normal distribution (especially for high-dimensional) and inaccuracy in acceptance rate estimation.  
 215        Fortunately, we found that a routine elliptical slice sampler (ESS)[36] works well due to its adaptive  
 216        bracket size and the fact that it changes the original high dimensional sampling problem to a one-  
 217        dimensional sampling problem of the angle  $\phi$ . ESS targets  $p(\psi) = \frac{1}{Z} \mathcal{N}(\psi; 0, \Sigma) L(\psi)$  which matches  
 218        the factorization in [Equation \(2.5\)](#). ESS proposes  $\psi' = \psi \sin \phi + \nu \cos \phi$  that lies on the ellipse based  
 219        on  $\psi$  and  $\nu \sim \mathcal{N}(0, \Sigma)$ , and its location depends on the angle  $\phi$ .  $\phi$  is then proposed uniformly from

220 a bracket  $[\phi_{min}, \phi_{max}]$  which is shrunk exponentially quickly until an acceptable state is found (221 i.e., the proposal  $\psi'$  lying in the likelihood threshold).

222 **To sample from**

223 (2.6) 
$$p(\theta|\boldsymbol{\lambda}, \{x_i\}_{i=1}^M) \propto p_\theta(\theta) \cdot \frac{\exp\left\{-\frac{1}{2}\boldsymbol{\lambda}'V_\theta^{-1}\boldsymbol{\lambda}\right\}}{\int_{\mathcal{F}} \exp\left\{-\frac{1}{2}\boldsymbol{\lambda}'V_\theta^{-1}\boldsymbol{\lambda}\right\} d\boldsymbol{\lambda}},$$

224 where  $\mathcal{F} = [0, +\infty)^{M+1}$ , we note that the term  $\int_{\mathcal{F}} \exp\left\{-\frac{1}{2}\boldsymbol{\lambda}'V_\theta^{-1}\boldsymbol{\lambda}\right\} d\boldsymbol{\lambda}$  in Equation (2.6) needs 225 to be numerically approximated, therefore simulating from this conditional posterior distribution 226 is a nontrivial problem. For example, HMC sampling from the full conditional of  $\theta$  is not directly 227 applicable here. However, in the case of Brownian motion covariance kernel with Gamma prior on 228  $\theta$ , we obtain conjugacy and it is possible to sample from Equation (2.6) directly. To show this, 229 consider the Brownian motion covariance kernel:  $V_\theta = \frac{1}{\theta} C$ , where

230 (2.7) 
$$C = \begin{pmatrix} x_1 & \dots & \min(x_1, x_M) & x_1 T - \frac{1}{2}x_1^2 \\ \vdots & \ddots & \vdots & \vdots \\ \min(x_M, x_1) & \dots & x_M & x_M T - \frac{1}{2}x_M^2 \\ x_1 T - \frac{1}{2}x_1^2 & \dots & x_M T - \frac{1}{2}x_M^2 & \frac{1}{3}T^3 \end{pmatrix}.$$

231 The marginal posterior now becomes

232 
$$p(\theta|\boldsymbol{\lambda}, \{x_i\}_{i=1}^M) \propto p_\theta(\theta) \cdot \frac{\exp\left\{-\frac{\theta}{2}\boldsymbol{\lambda}'C^{-1}\boldsymbol{\lambda}\right\}}{\int_{\mathcal{F}} \exp\left\{-\frac{\theta}{2}\boldsymbol{\lambda}'C^{-1}\boldsymbol{\lambda}\right\} d\boldsymbol{\lambda}}$$

233 
$$= p_\theta(\theta) \cdot \frac{\exp\left\{-\frac{\theta}{2}\boldsymbol{\lambda}'C^{-1}\boldsymbol{\lambda}\right\}}{\sqrt{\theta^{-(M+1)}} \int_{\mathcal{F}} \exp\left\{-\frac{1}{2}(\sqrt{\theta}\boldsymbol{\lambda})'C^{-1}(\sqrt{\theta}\boldsymbol{\lambda})\right\} d\sqrt{\theta}\boldsymbol{\lambda}}$$

234 
$$= p_\theta(\theta) \cdot \frac{\exp\left\{-\frac{\theta}{2}\boldsymbol{\lambda}'C^{-1}\boldsymbol{\lambda}\right\}}{\sqrt{\theta^{-(M+1)}} \int_{\mathcal{F}} \exp\left\{-\frac{1}{2}\mathbf{z}'C^{-1}\mathbf{z}\right\} d\mathbf{z}}$$

235 (2.8) 
$$\propto p_\theta(\theta) \cdot \sqrt{\theta}^{M+1} \exp\left\{-\frac{\theta}{2}\boldsymbol{\lambda}'C^{-1}\boldsymbol{\lambda}\right\},$$

236 where  $\mathbf{z} = \sqrt{\theta}\boldsymbol{\lambda}$ . The last step simplifies by noticing that the integral in the denominator no 237 longer depends on  $\theta$ . Setting  $p_\theta(\theta) = \Gamma(\alpha, \beta)$ , Equation (2.8) becomes a Gamma distribution with 238 parameters  $\tilde{\alpha} = \alpha + \frac{M+1}{2}$  and  $\tilde{\beta} = \beta + \frac{1}{2}\boldsymbol{\lambda}'C^{-1}\boldsymbol{\lambda}$ . In fact, this will also be the case for variance- 239 covariance matrices of the form  $\frac{1}{\theta}H_x$ , where  $H_x$  is a symmetric and positive definite matrix that 240 does not depend on  $\theta$ .

241 Generally, a Brownian motion kernel brings three computational advantages: (1) the integral 242 denominator now becomes analytical with respect to  $\theta$ , namely, a product of a constant and 243  $\sqrt{\theta}^{-(M+1)}$ ; (2) the conjugacy leads to a parametric marginal posterior distribution amenable for 244 Gibbs sampling; (3) we do not need to compute  $V_\theta$ ,  $V_\theta^{-1}$ , nor  $\text{chol}(V_\theta)$  for each iterative update of 245  $\theta$ , and instead we just need to compute  $C$ ,  $C^{-1}$ , and  $\text{chol}(C)$  only once. Moreover,  $C^{-1}$  is a tri- 246 diagonal matrix [42] amenable to fast sparse matrix computations of matrix inverse and Cholesky 247 decomposition.

248 A drawback of mean zero Brownian motion is that for function values at locations near the 249 origin, the prior places very small variance at these locations, and a strong influence in the posterior, 250 leading to low posterior values. To fix this problem, [42] proposed to use intrinsic Gaussian Markov 251 random fields priors with a proper correction at the boundary of the precision matrix  $C^{-1}$ . This is 252 equivalent to placing a noninformative prior on  $\lambda(0)$  and then marginalizing  $\lambda(0)$  out. In the rest 253 of this section we will show how to apply this boundary correction technique to derive a corrected 254 covariance.

255 First note that the distribution of  $\boldsymbol{\lambda}$  conditioned on  $\lambda(0) = y$  can be expressed as:

256 (2.9) 
$$p(\boldsymbol{\lambda} | \lambda(0) = y, \theta) \propto \exp \left\{ -\frac{\theta}{2} (\boldsymbol{\lambda} - y\mathbf{l})' C^{-1} (\boldsymbol{\lambda} - y\mathbf{l}) \right\} \mathbb{1}(\boldsymbol{\lambda} > \mathbf{0}),$$

257 where  $\mathbf{l} = (1, \dots, 1, T)'$ . Even though we conditioned on the initial value at  $y$ , i.e.,  $\lambda(0) = y$ ,  
258 the random walk density of  $\boldsymbol{\lambda}$  is expressed in terms of function differences  $\lambda(x_{i+1}) - \lambda(x_i) =$   
259  $\lambda(x_{i+1}) - y - (\lambda(x_i) - y)$ . This allows us to express the conditional density as a multivariate  
260 Gaussian distribution with shifted mean. Details are derived in [Appendix D](#). We then place a flat  
261 Gaussian prior on  $\lambda(0)$ ,  $\mathcal{N}(y; 0, \sigma^2)$ , with a large value of  $\sigma$ , and integrate  $\lambda(0)$  out to obtain the  
262 following modified random walk density:

263 (2.10) 
$$p(\boldsymbol{\lambda} | \theta) = \int_{-\infty}^{+\infty} p(\boldsymbol{\lambda} | \lambda(0) = y, \theta) \mathcal{N}(y; 0, \sigma^2) dy \approx \exp \left\{ -\frac{\theta}{2} \boldsymbol{\lambda}' \tilde{Q} \boldsymbol{\lambda} \right\} \mathbb{1}(\boldsymbol{\lambda} > \mathbf{0})$$

264 where  $\tilde{Q} = C^{-1} - \frac{C^{-1} \mathbf{l}' C^{-1}}{\mathbf{l}' C^{-1} \mathbf{l}}$ . Since  $\tilde{Q}$  is rank deficient, we usually add a small perturbation to  
265 its diagonal elements to obtain its inverse, i.e.,  $\tilde{C} = (\tilde{Q} + \epsilon \mathbf{I})^{-1}$ . Posterior sensitivity to different  
266 values of  $\epsilon$  is shown in [Appendix E](#). Although [Equation \(2.10\)](#) is obtained by taking the limit when  
267  $\sigma \rightarrow \infty$ , this serves as our motivation to define a new prior (not an approximation) with variance  
268 matrix  $\frac{1}{\theta} \tilde{C}$  instead of  $\frac{1}{\theta} C$ .

269 In our implementations, we simply replace  $C$  with  $\tilde{C}$  in [Equation \(2.8\)](#) and obtain

270 (2.11) 
$$p(\theta | \boldsymbol{\lambda}) \propto p_\theta(\theta) \cdot \sqrt{\theta}^{M+1} \exp \left\{ -\frac{\theta}{2} \boldsymbol{\lambda}' \tilde{C}^{-1} \boldsymbol{\lambda} \right\} = \Gamma \left( \alpha + \frac{M+1}{2}, \beta + \frac{1}{2} \boldsymbol{\lambda}' \tilde{C}^{-1} \boldsymbol{\lambda} \right)$$

271 To clarify, this intrinsic random walk with precision matrix boundary correction also corre-  
272 sponds to the first-order random walk utilized in the popular integrated nested Laplace approxi-  
273 mation model (INLA) [43], a baseline model we use for comparisons in [Section 3](#).

274 For other covariance kernels, we fix the value of  $\theta$  to an estimated value first and then we  
275 perform posterior sampling of  $\boldsymbol{\lambda}$  at locations of interest conditioned on  $\theta$  as in [Equation \(2.5\)](#).

276 **Estimation of  $\theta$ .** We first assume the intensity function is a piecewise constant function according  
277 to a regular grid of  $m - 1$  points. Denote the regular interval length as  $\Delta = \frac{T}{m-1}$ . The grid points  
278 are located at  $\left\{ \frac{2k-1}{2} \Delta \right\}_{k=1}^{m-1}$  and therefore we have  $m$  intervals in total, among which both the  
279 first and last intervals have a length of  $\frac{\Delta}{2}$ . The function values at each interval is denoted by  
280  $\boldsymbol{\lambda}_m^* = (\lambda_1^*, \dots, \lambda_m^*)$  and  $\Lambda_m^*$  denotes its corresponding cumulative intensity function. We then  
281 optimize the following:

282 (2.12) 
$$\arg \max_{m, \theta, \boldsymbol{\lambda}_m^*} (1 - c) \cdot \log(p(s_1, \dots, s_N | \boldsymbol{\lambda}_m^*)) + c \cdot \log(\mathcal{TN}(\boldsymbol{\lambda}_m^*, \Lambda_m^*; \mathbf{0}, V_\theta))$$

283 where  $c$  is a constant (set to be 0.2 in this work based on empirical observations). We name  
284 this procedure weighted MAP method. For a fixed value of  $m$ , we optimize over  $\boldsymbol{\lambda}_m^*$  and  $\theta$  using  
285 R-DEoptim [35]. We repeat this optimization procedure with different choices for  $m$  (e.g,  $m \in$   
286  $\{1, \dots, 10\}$ ) and end with the optimal value of [Equation \(2.12\)](#).

287 **Extending kernels to multiple dimensions.** For point processes observed in higher dimensions,  
288 [17] suggests two main kernel constructions, which can be obtained multiplying or adding uni-  
289 dimensional kernels. For 2-dimesional data  $(x_1, x_2), (x'_1, x'_2) \in \mathbb{R}^2$ , the product-kernel is defined as  
290  $k_1(x_1, x'_1) \times k_2(x_2, x'_2)$  and the additive-kernel is defined as  $k_1(x_1, x'_1) + k_2(x_2, x'_2)$ . Since a product-  
291 kernel offers more flexibility, we use it to model the intensity function for spatial data in the second  
292 real example in [Subsection 3.3](#). For a Brownian motion kernel, the product-kernel we use is the  
293 two-dimensional Brownian Sheet [38] with covariance kernel:

294 (2.13) 
$$k_{BS}((x_1, x_2), (x'_1, x'_2)) = \frac{1}{\theta} \min(x_1, x'_1) \cdot \min(x_2, x'_2)$$

295 A squared exponential kernel is directly applicable to high dimensional input spaces and categorized  
 296 as a product-kernel. The hyperparameters estimation and the posterior inference described above  
 297 for uni-dimensional input space is directly applicable to multi-dimensional input space (see the  
 298 two-dimensional case in [Subsection 3.3](#)). However, for higher-dimensional spaces, our proposed  
 299 MAP method becomes significantly more computationally intensive. Specifically, if we use  $m - 1$   
 300 grid points per dimension, then the size of the subspace (i.e., the size of  $\lambda_m^*$ ) scales as  $m^d$ , making  
 301 optimization over  $\lambda_m^*$  increasingly costly.

302 **3. Experiments.** In this section, we present two synthetic examples and three real examples  
 303 that consist of recurrent events, spatial point data, and mixed recurrent and count data. For  
 304 each synthetic example, we compare our proposed random integral (RI) method with the Sigmoid  
 305 Gaussian Cox Process method (SGCP) proposed by [2] and the INLA method [43]. Among the  
 306 three exact MCMC methods described in the introduction [2, 23, 44], only SGCP [2] provides open-  
 307 source code. In terms of computational efficiency, variational Bayes (VB) approaches and INLA are  
 308 popular choices, with INLA dominating in terms of citations and faster in terms of running time.  
 309 For example, Table 2 in [3] shows the running time of SGCP is 9 times longer than the variational  
 310 method STVB, while [Table 2](#) in our paper shows the running time of SGCP is 5800 times longer  
 311 than INLA.

312 We implement our algorithm in Python and run it on a shared computing cluster consisting of  
 313 24 CPU cores and 191 GB of memory and set a time limit of 7 days. For the RI method on temporal  
 314 data, we run a total of 50,000 iterations after 10,000 iterations of burn-in. For the SGCP model,  
 315 each iteration took more than 10,000 times longer than the RI method and for this reason, we were  
 316 only able to obtain about 10,000 iterations after 10,000 iterations of burn-in. However, some results  
 317 of the SGCP method shown in [Appendix E](#) could not be reported. For the second spatial data real  
 318 example in [Subsection 3.3](#) we run a total of 100,000 iterations after 100,000 iterations of burn-in.

319 **3.1. Simulations.** We simulated 100 realizations from a Poisson processes with each of the  
 320 following two intensities:

$$321 \quad (3.1) \quad \lambda_1(s) = 2 \exp\{-s/15\} + \exp\{-(s-25)/10)^2\}, \quad s \in [0, 50]. \\ 322 \quad (3.2) \quad \lambda_2(s) = 10, \quad s \in [0, 5].$$

323 For each realization and for all the three Bayesian inference methods (RI/SGCP/INLA), we as-  
 324 sumed a Brownian motion covariance kernel and placed a noninformative conjugate gamma prior  
 325 on the precision parameter  $\theta$  with hyperparameters  $\alpha = \beta = 0.1$ . Additionally, we ran both the  
 326 RI and SGCP methods with a squared exponential kernel and estimated hyperparamters with two  
 327 methods: (1) via the weighted MAP method (RI/SGCP-MAP), as described in [Subsection 2.3](#);  
 328 (2) the oracle MLE method (RI/SGCP-MLE) where hyperparameters of the squared exponential  
 329 kernel are estimated using the true intenstiy function values and observed events. We evaluated  
 330 the performance of these methods according to sum of squared errors (SSE), coverage, credible  
 331 intervals width and average running time among each 100 datasets (see their definitions in [Appen-](#)  
 332 [dix E](#)). We compared our Bayesian methods with the classical kernel smoothing (KS) approach  
 333 of [14, 4]. Specifically, we applied edge-corrected kernel smoothing using a squared-exponential  
 334 kernel and selected the bandwidth through several commonly used techniques: Poisson likelihood  
 335 cross-validation (PPL), Scott's rule (SCOTT), Diggle and Berman's [8] mean square error cross-  
 336 validation method (DIGGLE), and adaptive bandwidth (ADAPTIVE)[1, 12], all based on the R  
 337 code implementation spatstat [5] and sparr [13]. In addition to the simulations under the tra-  
 338 jectories of Equations (3.1) and (3.2), we tested our method on simulations with the intensities  
 339 of Equations (3.1) and (3.2) scaled by a factor of 2 and 3. Corresponding results can be found  
 340 in [Appendix E](#).

341 Results for one simulated dataset with intensities  $\lambda_1(s)$  and  $\lambda_2(s)$  ([Equation \(3.1\)](#)) are depicted  
 342 in [Figure 1](#), with squared exponential kernels ([Figure 1A](#)) and Brownian motion kernels ([Figure 1B](#)).

343 Although all Bayesian methods have comparable performance, INLA-BM (green shaded region in  
344 [Figure 1B](#)) shows higher uncertainty than any other method. This is consistent across 100 simula-  
345 tions, where INLA’s median credible interval width is 1.44 versus 1.20 with our method for  $\lambda_1(s)$   
346 and similarly for  $\lambda_2(s)$  (see [Table 1](#), first 3 rows, last column). Performance statistics based on 100  
347 simulations shown in [Table 1](#) indicate that our method is the best performing method among those  
348 based on Brownian motion kernels in terms of median SSE. Similarly, for squared exponential ker-  
349 nels with MAP hyperparameter estimation, our method outperforms SGCP in median SSE. Based  
350 on comparisons among the three Bayesian methods over the two synthetic examples, it is concluded  
351 that both RI and SGCP outperforms INLA, RI outperforming SGCP for most cases. Nonparamet-  
352 ric methods based on kernel smoothing with PPL and Scott bandwidth selection perform well in  
353 terms of SSE, while ADAPTIVE bandwidth kernel smoothing performs well in terms of coverage  
354 in the first synthetic example; however, they perform significantly worse than all Bayesian methods  
355 in the second synthetic example.

356 In all simulations, methods using Brownian motion kernels display larger uncertainty compared  
357 to those using squared exponential kernels. This may be due to the fact that hyperparameters of  
358 Brownian motion kernels are estimated within the MCMC procedure, while hyperparameters of  
359 squared exponential kernels are fixed with estimates. However, the median coverage of most meth-  
360 ods are larger than 95%, suggesting those methods are producing conservative credible intervals.  
361 Further, we report average running times among 100 simulated datasets per 10,000 iterations for  
362 all MCMC algorithms in both RI and SGCP methods for both synthetic examples in [Table 2](#). Even  
363 though the cluster used has 24 CPU cores, we parallelized by datasets and so the running times  
364 reported in [Table 2](#) correspond to time averages per dataset using a single CPU core. In addition,  
365 for INLA-BM, the reported running times are averages per dataset (not per iteration). Though  
366 INLA runs the fastest, RI achieved a large improvement over SGCP in terms of running time, which  
367 is comparable with INLA. For example, for intensity  $\lambda_1(s)$ , on average, INLA-BM takes 4.80 s in  
368 total and RI-BM takes 15.84 s in total, whereas SGCP-BM takes 13.97 hours in total.

369 **3.2. Earthquakes in Japan.** We are interested in estimating the intensity rate of earthquakes  
370 in Japan during the year 2019 with magnitude of at least 2.5. The dataset is gathered from the U.S.  
371 Geological Survey (2020)<sup>1</sup>, including 901 time points. Analogous to the synthetic examples, we run  
372 the RI model with both a Brownian motion covariance kernel and a squared exponential kernel  
373 and present the corresponding results in the top two panels of [Figure 2](#) (blue dashed lines). We  
374 observe that this earthquake temporal point process has a rate around 2.5, with a modest increase  
375 observed in the later time period.

376 **3.3. Redwoods.** We reanalyze the redwoods spatial dataset that consists of the locations of  
377 seedlings and saplings of California Giant Redwoods in a square sampling region (approximately 130  
378 feet across). It was first described and analysed by [46]. The R dataset ‘redwoodfull’ contains the  
379 full point pattern of 195 trees and the space area has been rescaled to the unit square  $[0, 1] \times [0, 1]$ .  
380 Here we use both the Brownian motion covariance kernel and the squared exponential kernel for GP  
381 priors on the intensity function. For a Brownian motion covariance kernel, in order to inherit its  
382 computation efficiency we resort to the two-dimensional Brownian Sheet with boundary correction  
383 as described in [Subsection 2.3](#). When we perform the boundary correction procedure, there exists  
384 a numerical problem related to the computation of  $C^{-1}$ , since the definition of the two-dimensional  
385 Brownian Sheet leads to very small diagonal elements in  $C$ . We have modified our code to first  
386 compute  $(aC)^{-1}$ , where  $a$  is a constant (e.g.,  $10^{12}$ ), then multiply by  $a$ .

387 Results are presented in the bottom two panels of [Figure 2](#). We observe that both methods  
388 capture spatial concentration patterns, though there is disagreement in some of the concentra-  
389 tions. In this example, we actually prefer squared exponential kernel as it allows for longer range  
390 dependencies.

---

<sup>1</sup>from the website <https://earthquake.usgs.gov/fdsnws/event/1/>

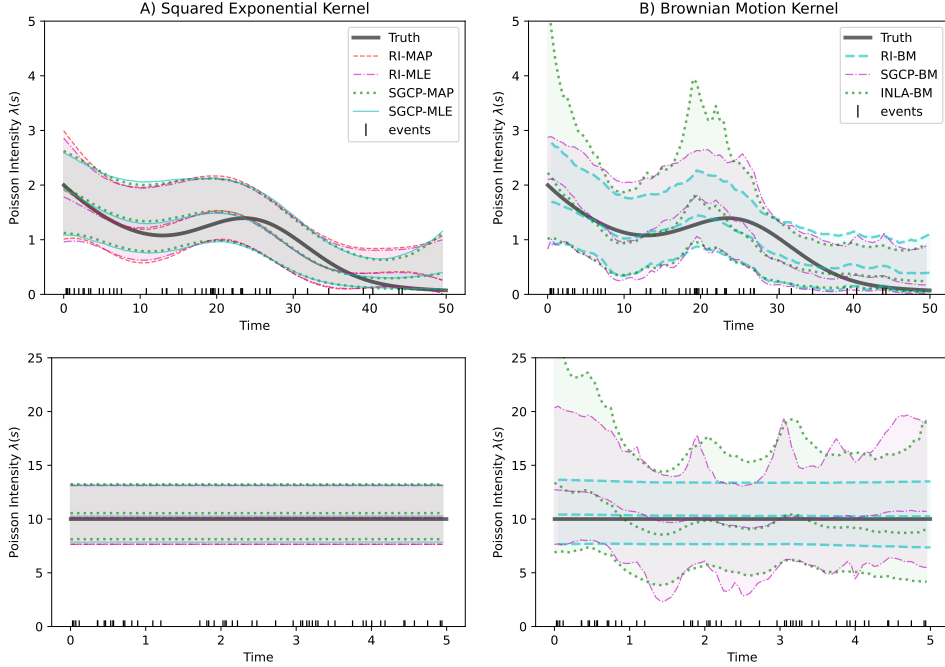


Figure 1: Top row corresponds to posterior inference of intensity function  $\lambda_1(s)$  from one simulated dataset of 50 events, while bottom row corresponds to posterior inference of intensity function  $\lambda_2(s)$  from one simulated dataset of 51 events. True trajectory is depicted by solid black curve, posterior medians by dashed central curves and 95% CI by shaded regions. Time of simulated events are shown as tick marks at the bottom of each plot. Different methods are distinguished by colors as described in legend boxes, and images in the same column share the same legend box. Methods used in panel A assume squared exponential kernels and those in panel B assume Brownian motion covariance kernels.

391     **3.4. Mixed recurrent and count data .** To exemplify the applicability of our methodology to  
 392 a mixture of recurrent event and count data, we modified the earthquake data previously analyzed  
 393 in Subsection 3.2. Specifically, we assume the exact recurrent event time points are observed within  
 394 the first 281 days and the rest of the year (84 days) is reported as weekly counts (12 weeks). In this  
 395 case, we a priori model the vector  $\tilde{\lambda} := [\lambda(x_1), \dots, \lambda(x_M), \int_{B_1} \lambda(s)ds, \dots, \int_{B_{12}} \lambda(s)ds]'$  as positive  
 396 multivariate Gaussian whose mean and covariance are described in Subsection 2.1. As before,  
 397  $\{x_i\}_{i=1}^M$  are the locations of interest, and the  $B_j$ s correspond to the weekly time intervals (from  
 398 ‘00:00:00’ of day 281+7( $j-1$ ) to ‘00:00:00’ of day 288+7( $j-1$ )). See its likelihood in Equation (2.2).  
 399 Posterior results are also depicted as red curves in the top panel of Figure 2. Remarkably, we obtain  
 400 very similar results to those obtained from the higher resolution recurrent event data (blue curves)  
 401 analyzed in Subsection 3.2.

402     **4. Discussion.** In this work, we propose an exact nonparametric Bayesian approach to estimate  
 403 the intensity function of an inhomogeneous Poisson process. The key insight in our method is the  
 404 realization that if the intensity function is a priori modeled as a Gaussian process, then the Poisson  
 405 likelihood is a function of a latent Gaussian vector consisting of intensity function values and  
 406 the cumulative intensity function over the observed set. Since the intensity function needs to be  
 407 positive, we further restrict the latent vector to being positive. This positive restriction, however,  
 408 does not increase the sampling complexity of our MCMC approach.

409     The greatest advantage of our method is that it does not require discretization, expensive data  
 410 augmentation, or variational approximations. Quite different from [29], which approximates the  
 411 cumulative intensity function via discretization, our method is exact and mainly focuses on solving  
 412 the doubly intractable posterior problem [37], though both utilize truncated Gaussian distributions.

Intensity	Methods	SSE at 100 Grids	Coverage at 100 Grids	Credible Interval Width
$\lambda_1$	RI-BM	<b>7.30</b> (5.22, 9.29)	98% (95%, 100%)	1.20 (1.15, 1.26)
	SGCP-BM	8.87 ( <b>5.19</b> , 12.54)	100% (100%, 100%)	1.35 (1.24, 1.43)
	INLA-BM	9.01 (6.18, 13.17)	100% (98%, 100%)	1.44 (1.31, 1.59)
	RI-MAP	<b>7.97</b> ( <b>5.60</b> , 11.51)	88% (72%, 99%)	0.84 (0.71, 1.03)
	SGCP-MAP	8.76 (6.73, <b>11.02</b> )	77% (59%, 89%)	0.84 (0.73, 0.99)
	RI-MLE	7.17 (4.49, <b>9.62</b> )	100% (94%, 100%)	1.04 (0.98, 1.07)
	SGCP-MLE	<b>6.33</b> ( <b>4.14</b> , 9.72)	100% (88%, 100%)	0.97 (0.93, 1.03)
	KS-PPL	7.70 (4.66, 11.01)	31% (19%, 51%)	0.25 (0.19, 0.39)
	KS-SCOTT	<b>6.18</b> ( <b>3.76</b> , 9.17)	32% (24%, 46%)	0.25 (0.23, 0.26)
$\lambda_2$	KS-DIGGLE	3178.84 (2684.54, 3596.24)	29% (26%, 31%)	10.30 (9.34, 11.36)
	KS-ADAPTIVE	10.35 (7.00, 14.49)	92% (83%, 98%)	1.05 (0.95, 1.12)
	RI-BM	<b>76.63</b> ( <b>28.65</b> , <b>220.65</b> )	100% (100%, 100%)	6.29 (5.95, 6.74)
	SGCP-BM	231.96 (106.33, 429.64)	100% (100%, 100%)	9.13 (8.56, 10.30)
	INLA-BM	328.58 (173.47, 570.52)	100% (100%, 100%)	12.04 (11.36, 12.90)
	RI-MAP	<b>121.56</b> (36.37, <b>298.73</b> )	100% (100%, 100%)	5.60 (5.26, 5.87)
	SGCP-MAP	145.73 ( <b>33.50</b> , 444.92)	100% (100%, 100%)	5.82 (5.43, 6.30)
	RI-MLE	<b>70.82</b> ( <b>21.04</b> , <b>216.55</b> )	100% (100%, 100%)	5.84 (5.41, 6.88)
	SGCP-MLE	105.56 ( <b>37.58</b> , 265.23)	100% (100%, 100%)	5.64 (5.30, 5.95)
	KS-PPL	500053.20 (267875.20, 847638.70)	88% (84%, 92%)	155.13 (118.26, 203.99)
	KS-SCOTT	<b>470.70</b> ( <b>252.59</b> , <b>784.66</b> )	100% (81%, 100%)	7.79 (7.17, 8.15)
	KS-DIGGLE	868245.30 (450177.00, 1693187.20)	87% (82%, 91%)	202.95 (153.87, 279.27)
	KS-ADAPTIVE	728.72 (468.86, 1178.17)	100% (91%, 100%)	12.28 (11.30, 13.15)

Table 1: x-BM refers to method x using a Brownian motion kernel. x-MAP denotes method x with a squared exponential kernel, where the hyperparameters are estimated via a weighted MAP approach. x-MLE denotes method x with a squared exponential kernel, where the hyperparameters are estimated using an oracle MLE approach—that is, based on the true intensity function values and observed events. KS-x denotes the kernel smoothing approach with a squared-exponential kernel, where x indicates the method used for bandwidth selection. Performance comparison over 100 grids (test points) on 100 simulations with intensities  $\lambda_1(s)$  and  $\lambda_2(s)$ . The last three columns present quantities in the format: 0.50 quantile (0.25 quantile, 0.75 quantile). Bold is the best among methods with the same kernel. Details of metric definitions and calculations are in [Appendix E](#).

413 Discretization results in poor approximation, especially in high dimensions, as the choice of the  
414 number of knots controls the trade-off between numerical accuracy and computational efficiency.  
415 This problem is exacerbated when data consists of mixed recurrent event and count data as many  
416 integrals would need to be approximated. Further, as mentioned earlier in [Subsection 2.3](#), we use a  
417 different but more efficient MCMC scheme than [\[29\]](#). Our proposed method is most similar to both  
418 [\[23\]](#) and [\[44\]](#), in that we treat the cumulative intensity function as a latent random variable, and  
419 target a posterior distribution augmented by the cumulative intensity function. Both [\[23\]](#) and [\[44\]](#)  
420 reduce time complexity from cubic in the number of both thinning and observed data points in [\[2\]](#)  
421 to linear in the number of observed data points for each MCMC iteration. In our proposed method,  
422 attributed to the special structure of Brownian motion kernel covariance, we only need to compute  
423 all covariance matrices once during the MCMC procedure, bringing improvement in time efficiency.  
424 Specifically, [\[2\]](#) has a time complexity of  $O(t(M + S)^3)$ , [\[44\]](#) scales computationally in  $O(tMk^2)$ ,  
425 while the time complexity under our method is  $\max(O(M^3), O(tM^2))$ , where  $t$  denotes the number  
426 of iterations,  $S$  denotes the expected number of latent thinning points, and  $k$  denotes the number of  
427 inducing points. On the other hand, one limitation of our approach is the requirement of integrable  
428 covariance kernels.

429 Data augmentation methods via Poisson thinning [\[2, 16\]](#) require a finite bound and a tractable  
430 acceptance probability, restricting its applicability. For example, [\[50\]](#) mentions the bottleneck of  
431 applying the data augmentation via thinning method to renewal processes with unbounded hazard  
432 functions. In contrast, the random integral method can handle both unbounded and more complex  
433 intractable cases. A future direction consists in extending the random integral method to more  
434 general point processes such as those used in survival analysis [\[6, 18, 30\]](#). We anticipate our method  
435 will be able to naturally accommodate censored data and spatio-temporally varying covariates.

Methods	Average Time $\pm$ Standard Deviation	
	$\lambda_1$	$\lambda_2$
RI-BM	$2.64 \pm 0.11$ s	$2.28 \pm 0.90$ s
SGCP-BM	$28146.07 \pm 4862.67$ s	$5724.21 \pm 1025.27$ s
INLA-BM	$4.80 \pm 0.19$ s	$4.51 \pm 1.02$ s
RI-MAP	$3.17 \pm 0.44$ s	$3.58 \pm 0.98$ s
SGCP-MAP	$127598.22 \pm 36866.47$ s	$41339.5 \pm 12600.63$ s
RI-MLE	$3.49 \pm 0.33$ s	$2.79 \pm 0.27$ s
SGCP-MLE	$169883.37 \pm 28625.97$ s	$41057.43 \pm 8801.7$ s
KS-PPL	$0.09 \pm 0.04$ s	$0.09 \pm 0.05$ s
KS-SCOTT	$0.06 \pm 0.04$ s	$0.07 \pm 0.04$ s
KS-DIGGLE	$0.11 \pm 0.06$ s	$0.08 \pm 0.04$ s
KS-ADAPTIVE	$537.62 \pm 190.47$ s	$319.52 \pm 166.12$ s

Table 2: Average running times across 100 simulated datasets for estimating  $\lambda_1(s)$  and  $\lambda_2(s)$ .

436 Finally, we showed that our method can be extended to model mixed data consisting of re-  
 437 current event data and count data over binned intervals. Surprisingly, we showed an example in  
 438 which binning some of the observations resulted in no loss of information about the intensity func-  
 439 tion. This feature not only increases the applicability of nonparametric Bayesian Cox processes to  
 440 more realistic scenarios, but it can also be exploited for increasing scalability of our method. We  
 441 anticipate that it is possible to devise a strategy for binning observations in order to increase the  
 442 applicability of our method to large datasets.

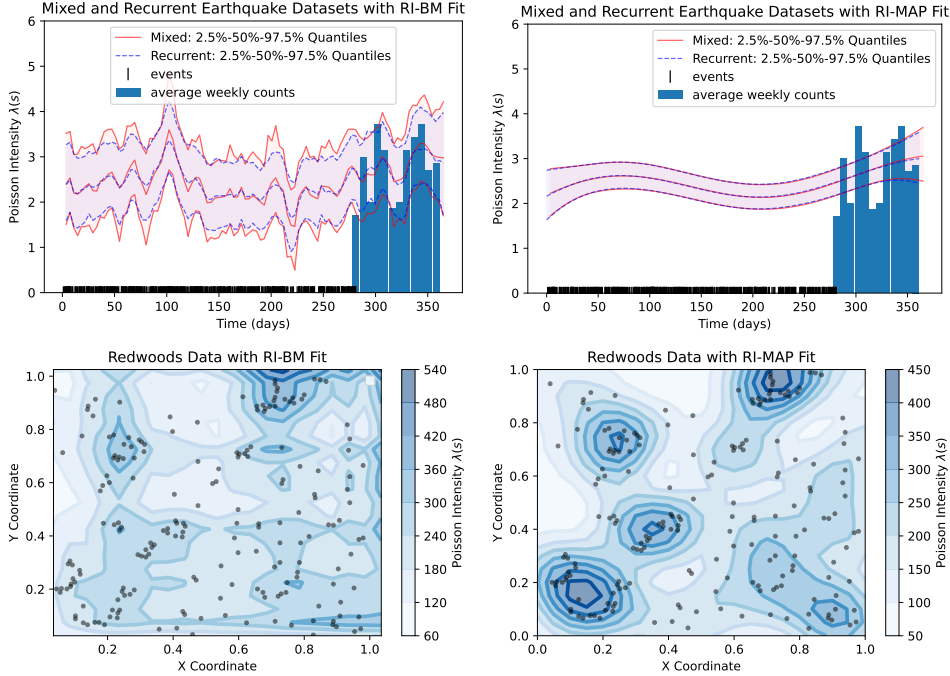


Figure 2: Posterior inferences for real examples from Subsections 3.2 to 3.4. Bottom panels report median among posterior samples of the latent GP for the redwoods spatial dataset and locations of observed events are represented by black dots, while top panels present 2.5% – 50% – 97.5% posterior quantiles of the intensity function for both recurrent and mixed earthquake data in Japan and time of observed events are depicted as tick marks at the bottom of each plot. Among each row, the left panel corresponds to results using a Brownian motion covariance kernel and the right panel corresponds to results using a squared exponential kernel with MAP.

443     **Appendix A. joint distribution of function values and integral for Gaussian processes.** First,  
 444 we state a key intermediate result from [34] that we will use to prove [Theorem 2.1](#):

445     **Proposition A.1.** [*Proposition 12.15 in [34]*] Suppose  $\{X_n : n \in N\}$  is a sequence of Gaussian  
 446 random vectors and  $X_n \xrightarrow{a.s.} X$ . If  $b := \lim_{n \rightarrow \infty} E[X_n]$  and  $C := \lim_{n \rightarrow \infty} \text{Cov}[X_n]$  exist, then  $X$  is  
 447 Gaussian with mean  $b$  and covariance matrix  $C$ .

448     **Proof.** Let  $\mu_n$  denote  $E[X_n]$ ,  $\Sigma_n$  denote  $\text{Cov}[X_n]$ , and  $\psi$  denote the characteristic function.  
 449 Since  $X_n \xrightarrow{a.s.} X$  implies that  $\psi_{X_n}(t) \rightarrow \psi_X(t)$  for each  $t$ , the rest work is to derive  $\lim_{n \rightarrow \infty} \psi_{X_n}(t)$ .

$$450 \quad \lim_{n \rightarrow \infty} \psi_{X_n}(t) = \lim_{n \rightarrow \infty} \exp \left\{ it' \mu_n - \frac{1}{2} t' \Sigma_n t \right\} \\ 451 \quad = \exp \left\{ it' b - \frac{1}{2} t' C t \right\}$$

The last step is due to the continuity of  $\exp \{it' \mu_n - \frac{1}{2} t' \Sigma_n t\}$  w.r.t. components of  $\mu_n$  and  $\Sigma_n$ . Now we have

$$\psi_X(t) = \exp \left\{ it' b - \frac{1}{2} t' C t \right\}.$$

452 The result then follows. ■

453     **Theorem 2.1.** Suppose the Gaussian process  $f(\cdot)$  on the compact space  $\mathcal{X}$  satisfies the assumption  
 454 that its mean function  $\mu(\cdot)$  and covariance kernel  $k(\cdot, \cdot)$  are integrable, i.e.,  $\int_{\mathcal{X}} \mu(s) ds, \int_{\mathcal{X}} k(s, t) dt$   
 455 and  $\int \int_{\mathcal{X} \times \mathcal{X}} k(s, t) ds dt$  exist. For every finite set of vectors  $s_1, \dots, s_p \in \mathcal{X}$ , the vector  $\mathbf{f} :=$

456  $[f(s_1), \dots, f(s_p), \int_{\mathcal{X}} f(s)ds]'$  follows a Gaussian distribution and

457  $\mathbf{f} \sim \mathcal{N}\left(\boldsymbol{\mu}, \begin{pmatrix} \mathbf{V}_{SS} & \mathbf{V}_{SI} \\ \mathbf{V}'_{SI} & \mathbf{V}_{II} \end{pmatrix}\right),$

458 where  $\boldsymbol{\mu} := [\mu(s_1), \dots, \mu(s_p), \int_{\mathcal{X}} \mu(s)ds]', \mathbf{V}_{SS}$  is the  $p \times p$  kernel matrix containing covariance  
 459 terms for all pairs of function values  $\{f(s_i)\}_{i=1}^p, \mathbf{V}_{SI}$  is a  $p$ -dimensional vector formed by covariance  
 460 terms between function values  $\{f(s_i)\}_{i=1}^p$  and  $\int_{\mathcal{X}} f(s)ds$  with  $i$ -th term being  $\int_{\mathcal{X}} k(s_i, t)dt$ , and  $\mathbf{V}_{II}$   
 461 is the covariance of  $\int_{\mathcal{X}} f(s)ds$ , whose value is  $\int_{\mathcal{X} \times \mathcal{X}} k(s, t)dsdt$ .

462 **Proof.** It is well known that any affine transformation of a multivariate normal distribution is  
 463 still a normal distribution. That is to say, if  $X \sim \mathcal{N}(X; \boldsymbol{\mu}, \Sigma)$ , then  $BX \sim \mathcal{N}(BX; B\boldsymbol{\mu}, B\Sigma B')$ ,  
 464 where  $X$  is a  $n$ -dimensional random vector and  $B$  is a  $m \times n$  constant matrix.

For presentation simplicity, here we only focus on the case when  $\mathcal{X} = [0, T]$ , i.e., an uni-dimensional space. The proof can be easily extended to a higher finite dimension. Because  $f(s)$  is a continuous function, we can define the integral term  $\int_{\mathcal{X}} f(s)ds$  as the limit of the Riemann sum:

$$\int_0^T f(s)ds := \lim_{n \rightarrow \infty} \frac{T}{n} \sum_{i=1}^n f\left(\frac{i}{n}T\right).$$

465 Now, define  $X_n = (f(s_1), \dots, f(s_p), f(\frac{1}{n}T), \dots, f(T))'$ , then

466  $X_n \sim \mathcal{N}\left(\tilde{\boldsymbol{\mu}}_n = \begin{pmatrix} \mu(s_1) \\ \vdots \\ \mu(s_p) \\ \mu(\frac{1}{n}T) \\ \vdots \\ \mu(T) \end{pmatrix}, \tilde{\Sigma}_n = \begin{pmatrix} k(s_1, s_1) & \dots & k(s_1, s_p) & k(s_1, \frac{1}{n}T) & \dots & k(s_1, T) \\ \vdots & \ddots & \vdots & \vdots & \ddots & \vdots \\ k(s_p, s_1) & \dots & k(s_p, s_p) & k(s_p, \frac{1}{n}T) & \dots & k(s_p, T) \\ k(\frac{1}{n}T, s_1) & \dots & k(\frac{1}{n}T, s_p) & k(\frac{1}{n}T, \frac{1}{n}T) & \dots & k(\frac{1}{n}T, T) \\ \vdots & \ddots & \vdots & \vdots & \ddots & \vdots \\ k(T, s_1) & \dots & k(T, s_p) & k(T, \frac{1}{n}T) & \dots & k(T, T) \end{pmatrix}\right)$

467 Let  $A = \begin{pmatrix} \mathbf{I}_{p \times p} & \mathbf{0}_{p \times n} \\ \mathbf{0}_{1 \times p} & (\frac{T}{n})_{1 \times n} \end{pmatrix}$ , then  $AX_n = \begin{pmatrix} f(s_1) \\ \vdots \\ f(s_p) \\ \frac{T}{n} \sum_{i=1}^n f\left(\frac{i}{n}T\right) \end{pmatrix} \xrightarrow{a.s.} \begin{pmatrix} f(s_1) \\ \vdots \\ f(s_p) \\ \int_0^T f(s)ds \end{pmatrix}.$

Since  $AX_n$  is an affine transformation of a multivariate normal distribution,

$$AX_n \sim \mathcal{N}(A\tilde{\boldsymbol{\mu}}_n, A\tilde{\Sigma}_n A'),$$

468 where  $A\tilde{\boldsymbol{\mu}}_n = \begin{pmatrix} \mu(s_1) \\ \vdots \\ \mu(s_p) \\ \frac{T}{n} \sum_{i=1}^n \mu\left(\frac{i}{n}T\right) \end{pmatrix} \xrightarrow{n \rightarrow \infty} \begin{pmatrix} \mu(s_1) \\ \vdots \\ \mu(s_p) \\ \int_0^T \mu(s)ds \end{pmatrix},$

469 and  $A\tilde{\Sigma}_n A' = \begin{pmatrix} k(s_1, s_1) & \dots & k(s_1, s_p) & \frac{T}{n} \sum_{i=1}^n k\left(s_1, \frac{i}{n}T\right) \\ \vdots & \ddots & \vdots & \vdots \\ k(s_p, s_1) & \dots & k(s_p, s_p) & \frac{T}{n} \sum_{i=1}^n k\left(s_p, \frac{i}{n}T\right) \\ \frac{T}{n} \sum_{i=1}^n k\left(\frac{i}{n}T, s_1\right) & \dots & \frac{T}{n} \sum_{i=1}^n k\left(\frac{i}{n}T, s_p\right) & \left(\frac{T}{n}\right)^2 \sum_{j=1}^n \sum_{i=1}^n k\left(\frac{i}{n}T, \frac{j}{n}T\right) \end{pmatrix}$   
 470  $\xrightarrow{n \rightarrow \infty} \begin{pmatrix} k(s_1, s_1) & \dots & k(s_1, s_p) & \int_0^T k(s_1, t)dt \\ \vdots & \ddots & \vdots & \vdots \\ k(s_p, s_1) & \dots & k(s_p, s_p) & \int_0^T k(s_p, t)dt \\ \int_0^T k(t, s_1)dt & \dots & \int_0^T k(t, s_p)dt & \int_0^T \int_0^T k(s, t)dsdt \end{pmatrix}.$

471 The result then follows from [Proposition A.1](#). ■

Pairs of samples	KL Divergence
L=20 vs. L=100	2.159529e-07
L=100 vs. L=200	1.715119e-06
L=200 vs. L=300	3.163985e-07

Table 3: KL divergence for each pair of marginal density estimates on  $\lambda(s_1)$ .

**Appendix B. empirical asymptotic convergence of the positive Gaussian prior.** To evaluate how sensitive our induced marginal prior on  $\lambda_N$  is to the prediction set, we estimated different marginal priors via Monte Carlo. We assumed  $(\lambda(s_1), \{\lambda(t_l)\}_{l=1}^L) \sim \mathcal{TN}(\mathbf{0}, \Sigma)$ , where  $s_1 = 0.31$  and  $\{\lambda(t_l)\}_{l=1}^L$  at evenly spaced grids in  $[0, 1]$ . We assumed squared exponential kernel for  $\Sigma$  and set  $L = 20, 100, 200, 300$ . The estimated marginal densities of  $\lambda(s_1)$  and KL divergences for each pair of them are presented in Figure 3 and Table 3. We conclude from both qualitative and quantitative results that, if  $\{\lambda(t_l)\}_{l=1}^L$  is dense in  $\mathcal{S}$  and  $p(\{\lambda(s_i)\}_{i=1}^N, \{\lambda(t_l)\}_{l=1}^L)$  follows a truncated positive Gaussian distribution, then the limiting induced marginal exists, that is

$$\lim_{L \rightarrow \infty} \int_{\otimes_{i=1}^L [0, +\infty)} \mathcal{TN}\left(\{\lambda(s_i)\}_{i=1}^N, \{\lambda(t_l)\}_{l=1}^L\right) d\{\lambda(t_l)\}_{l=1}^L$$

473 exists.

474 **Appendix C. kernel integral.** In this section, we would show how to derive the integral terms  
475 in the covariance matrix in Theorem 2.1 for two specific kernel functions.

476 **C.1. Squared exponential kernels .** For a Gaussian process with a squared exponential kernel,  
477 here we show the derivation for  $\int_0^T k_{SE}(s, t) dt$  and  $\int_0^T \int_0^T k_{SE}(s, t) ds dt$ . We first claim three facts  
478 about the Gauss error function  $erf(z) := \frac{2}{\sqrt{\pi}} \int_0^z \exp\{-t^2\} dt$ .

479 **FACT 1:**  $\int_p^q \exp\left\{-\frac{x^2}{2}\right\} dx = \sqrt{\frac{\pi}{2}} (erf(q/\sqrt{2}) - erf(p/\sqrt{2}))$

480 **FACT 2:**  $\int erf(z) dz = z erf(z) + \frac{\exp\{-z^2\}}{\sqrt{\pi}} + c$

481 **FACT 3:**  $erf(-z) = -erf(z)$

482 Utilizing the three facts, we compute both single and double integral terms as below.

$$\begin{aligned}
 484 \quad & \int_0^T k_{SE}(s, t) dt = \int_0^T \theta_0 \exp\left(-\frac{\theta_1(s-t)^2}{2}\right) dt \\
 485 \quad & = \frac{\theta_0}{\sqrt{\theta_1}} \int_0^T \exp\left(-\frac{\theta_1(t-s)^2}{2}\right) d\sqrt{\theta_1}(t-s) \\
 486 \quad & = \frac{\theta_0}{\sqrt{\theta_1}} \int_{-\sqrt{\theta_1}s}^{\sqrt{\theta_1}(T-s)} \exp\left\{-\frac{v^2}{2}\right\} dv \\
 487 \quad & = \frac{\theta_0}{\sqrt{\theta_1}} \sqrt{\frac{\pi}{2}} \left[ erf\left(\sqrt{\frac{\theta_1}{2}}(T-s)\right) - erf\left(-\sqrt{\frac{\theta_1}{2}}s\right) \right] \\
 488 \quad & = \theta_0 \sqrt{\frac{\pi}{2\theta_1}} \left[ erf\left(\sqrt{\frac{\theta_1}{2}}(T-s)\right) + erf\left(\sqrt{\frac{\theta_1}{2}}s\right) \right]
 \end{aligned}$$

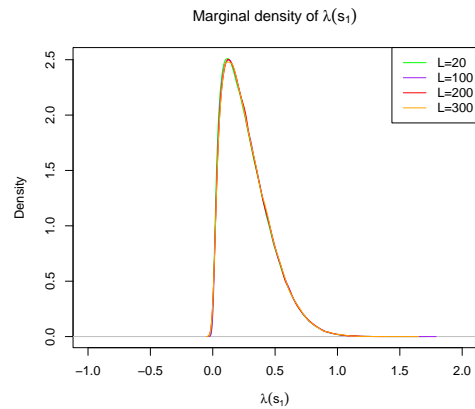


Figure 3: Marginal density estimates for  $\lambda(s_1)$  corresponding to  $L = 20, 100, 200, 300$ .

489 where  $v := \sqrt{\theta_1}(t - s)$ .

$$\begin{aligned}
490 \quad & \int_0^T \int_0^T k_{SE}(s, t) dt ds = \int_0^T \theta_0 \sqrt{\frac{\pi}{2\theta_1}} \left[ \operatorname{erf} \left( \sqrt{\frac{\theta_1}{2}} (T - s) \right) + \operatorname{erf} \left( \sqrt{\frac{\theta_1}{2}} s \right) \right] ds \\
491 \quad & = \theta_0 \sqrt{\frac{\pi}{2\theta_1}} \left[ \int_0^T \operatorname{erf} \left( \sqrt{\frac{\theta_1}{2}} (T - s) \right) ds + \int_0^T \operatorname{erf} \left( \sqrt{\frac{\theta_1}{2}} s \right) ds \right] \\
492 \quad & = \theta_0 \sqrt{\frac{\pi}{2\theta_1}} \left[ -\sqrt{\frac{2}{\theta_1}} \int_0^T \operatorname{erf} \left( \sqrt{\frac{\theta_1}{2}} (T - s) \right) d\sqrt{\frac{\theta_1}{2}} (T - s) + \sqrt{\frac{2}{\theta_1}} \int_0^T \operatorname{erf} \left( \sqrt{\frac{\theta_1}{2}} s \right) d\sqrt{\frac{\theta_1}{2}} s \right] \\
493 \quad & = \theta_0 \sqrt{\frac{\pi}{2\theta_1}} \left[ -\sqrt{\frac{2}{\theta_1}} \int_0^T \operatorname{erf} \left( \sqrt{\frac{\theta_1}{2}} (T - s) \right) d\sqrt{\frac{\theta_1}{2}} (T - s) + \sqrt{\frac{2}{\theta_1}} \int_0^T \operatorname{erf} \left( \sqrt{\frac{\theta_1}{2}} s \right) d\sqrt{\frac{\theta_1}{2}} s \right] \\
494 \quad & = \frac{\sqrt{\pi}\theta_0}{\theta_1} \left[ \int_0^{\sqrt{\frac{\theta_1}{2}} T} \operatorname{erf}(u) du + \int_0^{\sqrt{\frac{\theta_1}{2}} T} \operatorname{erf}(v) dv \right] \\
495 \quad & = \frac{2\sqrt{\pi}\theta_0}{\theta_1} \left[ u \operatorname{erf}(u) + \frac{\exp\{-u^2\}}{\sqrt{\pi}} \Big|_0^{\sqrt{\frac{\theta_1}{2}} T} \right] \\
496 \quad & = \frac{2\sqrt{\pi}\theta_0}{\theta_1} \left[ \sqrt{\frac{\theta_1}{2}} T \operatorname{erf} \left( \sqrt{\frac{\theta_1}{2}} T \right) + \frac{\exp\left\{-\frac{\theta_1}{2} T^2\right\}}{\sqrt{\pi}} - \frac{1}{\sqrt{\pi}} \right] \\
497 \quad & = \frac{2\theta_0}{\theta_1} \left[ \sqrt{\frac{\pi\theta_1}{2}} T \operatorname{erf} \left( \sqrt{\frac{\theta_1}{2}} T \right) + \exp\left\{-\frac{\theta_1}{2} T^2\right\} - 1 \right]
\end{aligned}$$

■

498 where  $u := \sqrt{\frac{\theta_1}{2}}(T - s)$  and  $v := \sqrt{\frac{\theta_1}{2}}s$ .

499      **C.2. Brownian motion covariance kernels.** Next, we would show a similar derivation for a  
500    Gaussian process with a Brownian motion covariance kernel.

501      
$$\int_0^T k_{BM}(s, t) dt = \int_0^T \frac{1}{\theta} \min(s, t) dt = \frac{1}{\theta} \left[ \int_0^s t dt + \int_s^T s dt \right]$$

502      
$$= \frac{1}{\theta} \left[ \frac{1}{2} t^2 \Big|_0^s + st \Big|_s^T \right] = \frac{1}{\theta} \left( sT - \frac{1}{2} s^2 \right)$$

503

504      
$$\int_0^T \int_0^T k_{BM}(s, t) dt ds = \int_0^T \frac{1}{\theta} \left( sT - \frac{1}{2} s^2 \right) ds$$

505      
$$= \frac{1}{\theta} \left( \frac{1}{2} Ts^2 - \frac{1}{6} s^3 \right) \Big|_0^T = \frac{1}{3\theta} T^3$$

506      **Appendix D. Brownian motion precision matrix boundary correction.** We first show how to  
507    derive  $p(\boldsymbol{\lambda} | \lambda(0) = y, \theta)$  in [Equation \(2.9\)](#). For a Brownian motion starting at  $y$ , the conditional  
508    distribution of  $(\lambda(x_1), \dots, \lambda(x_M))$  given  $\lambda(0) = y$  is:

509      
$$p(\lambda(x_1), \dots, \lambda(x_M) | \lambda(0) = y, \theta) \propto \exp \left\{ -\frac{\theta}{2} \left[ \frac{(\lambda(x_{(1)}) - y)^2}{x_{(1)}} + \sum_{i=2}^M \frac{[\lambda(x_{(i)}) - \lambda(x_{(i-1)})]^2}{x_{(i)} - x_{(i-1)}} \right] \right\}$$

510      
$$= \exp \left\{ -\frac{\theta}{2} \begin{pmatrix} \lambda(x_{(1)}) - y \\ \vdots \\ \lambda(x_{(M)}) - y \end{pmatrix}' Q \begin{pmatrix} \lambda(x_{(1)}) - y \\ \vdots \\ \lambda(x_{(M)}) - y \end{pmatrix} \right\}$$

511      (D.1)      
$$= \exp \left\{ -\frac{\theta}{2} \begin{pmatrix} \lambda(x_1) - y \\ \vdots \\ \lambda(x_M) - y \end{pmatrix}' \Sigma^{-1} \begin{pmatrix} \lambda(x_1) - y \\ \vdots \\ \lambda(x_M) - y \end{pmatrix} \right\}$$

512    where  $x_{(1)}, \dots, x_{(M)}$  are the increasingly ordered locations of  $x_1, \dots, x_M$ ,  $Q$  is a symmetric matrix

513    with components  $Q_{ij} = \begin{cases} \frac{1}{x_{(1)}} + \frac{1}{x_{(2)} - x_{(1)}} & \text{if } i = j = 1 \\ \frac{1}{x_{(i+1)} - x_{(i)}} + \frac{1}{x_{(i)} - x_{(i-1)}} & \text{if } 1 < i = j < M \\ \frac{1}{x_{(M)} - x_{(M-1)}} & \text{if } i = j = M \\ -\frac{1}{x_{(i+1)} - x_{(i)}} & \text{if } j = i + 1 \\ 0 & \text{otherwise} \end{cases}$ ,

514    and  $\Sigma = \begin{pmatrix} x_1 & \dots & \min(x_1, x_M) \\ \vdots & \ddots & \vdots \\ \min(x_M, x_1) & \dots & x_M \end{pmatrix}$ .

515    Derived from [Equation \(D.1\)](#) and [Theorem 2.1](#), we obtain  $p(\boldsymbol{\lambda} | \lambda(0) = y, \theta)$  as below.

516      
$$p(\boldsymbol{\lambda} | \lambda(0) = y, \theta) \propto \exp \left\{ -\frac{\theta}{2} \begin{pmatrix} \lambda(x_1) - y \\ \vdots \\ \lambda(x_M) - y \\ \int_0^T \lambda(s) ds - Ty \end{pmatrix}' C^{-1} \begin{pmatrix} \lambda(x_1) - y \\ \vdots \\ \lambda(x_M) - y \\ \int_0^T \lambda(s) ds - Ty \end{pmatrix} \right\}$$

517      
$$= \exp \left\{ -\frac{\theta}{2} (\boldsymbol{\lambda} - y\mathbf{l})' C^{-1} (\boldsymbol{\lambda} - y\mathbf{l}) \right\}$$

518 where  $\mathbf{l} = (1, \dots, 1, T)'$  and  $C$  is the same as [Equation \(2.7\)](#).

519 Next, we will show how to derive the distribution of a positive truncated random walk, after  
520 boundary correction, corresponding to [Equation \(2.10\)](#).

$$\begin{aligned}
521 \quad & p(\boldsymbol{\lambda} | \theta) \\
522 \quad &= \int_{-\infty}^{+\infty} p(\boldsymbol{\lambda} | \lambda(0) = y, \theta) \mathcal{N}(y; 0, \sigma^2) dy \\
523 \quad &\propto \mathbb{1}(\boldsymbol{\lambda} > \mathbf{0}) \int_{-\infty}^{+\infty} \exp \left\{ -\frac{\theta}{2} \left[ (\mathbf{y}\mathbf{l} - \boldsymbol{\lambda})' C^{-1} (\mathbf{y}\mathbf{l} - \boldsymbol{\lambda}) + \frac{y^2}{\theta\sigma^2} \right] \right\} dy \\
524 \quad &= \mathbb{1}(\boldsymbol{\lambda} > \mathbf{0}) \int_{-\infty}^{+\infty} \exp \left\{ -\frac{\theta}{2} \left[ y^2 \left( \mathbf{l}' C^{-1} \mathbf{l} + \frac{1}{\theta\sigma^2} \right) - 2y\mathbf{l}' C^{-1} \boldsymbol{\lambda} + \boldsymbol{\lambda}' C^{-1} \boldsymbol{\lambda} \right] \right\} dy \\
525 \quad &= \mathbb{1}(\boldsymbol{\lambda} > \mathbf{0}) \int_{-\infty}^{+\infty} \exp \left\{ -\frac{\theta}{2} \left[ \left( \mathbf{l}' C^{-1} \mathbf{l} + \frac{1}{\theta\sigma^2} \right) \left( y - \frac{\mathbf{l}' C^{-1} \boldsymbol{\lambda}}{\mathbf{l}' C^{-1} \mathbf{l} + \frac{1}{\theta\sigma^2}} \right)^2 + \boldsymbol{\lambda}' C^{-1} \boldsymbol{\lambda} - \frac{(\mathbf{l}' C^{-1} \boldsymbol{\lambda})^2}{\mathbf{l}' C^{-1} \mathbf{l} + \frac{1}{\theta\sigma^2}} \right] \right\} dy \\
526 \quad &= \mathbb{1}(\boldsymbol{\lambda} > \mathbf{0}) \exp \left\{ -\frac{\theta}{2} \left[ \boldsymbol{\lambda}' C^{-1} \boldsymbol{\lambda} - \frac{(\mathbf{l}' C^{-1} \boldsymbol{\lambda})^2}{\mathbf{l}' C^{-1} \mathbf{l} + \frac{1}{\theta\sigma^2}} \right] \right\} \int_{-\infty}^{+\infty} \exp \left\{ -\frac{\theta (\mathbf{l}' C^{-1} \mathbf{l} + \frac{1}{\theta\sigma^2})}{2} \left( y - \frac{\mathbf{l}' C^{-1} \boldsymbol{\lambda}}{\mathbf{l}' C^{-1} \mathbf{l} + \frac{1}{\theta\sigma^2}} \right)^2 \right\} dy \\
527 \quad &= \mathbb{1}(\boldsymbol{\lambda} > \mathbf{0}) \exp \left\{ -\frac{\theta}{2} \left[ \boldsymbol{\lambda}' C^{-1} \boldsymbol{\lambda} - \frac{(\mathbf{l}' C^{-1} \boldsymbol{\lambda})^2}{\mathbf{l}' C^{-1} \mathbf{l} + \frac{1}{\theta\sigma^2}} \right] \right\} \left( \theta \mathbf{l}' C^{-1} \mathbf{l} + \frac{1}{\sigma^2} \right)^{-\frac{1}{2}} \int_{-\infty}^{+\infty} \exp \left\{ -\frac{z^2}{2} \right\} dz \\
528 \quad &\propto \mathbb{1}(\boldsymbol{\lambda} > \mathbf{0}) \exp \left\{ -\frac{\theta}{2} \left[ \boldsymbol{\lambda}' C^{-1} \boldsymbol{\lambda} - \frac{(\mathbf{l}' C^{-1} \boldsymbol{\lambda})^2}{\mathbf{l}' C^{-1} \mathbf{l} + \frac{1}{\theta\sigma^2}} \right] \right\} \\
529 \quad &= \mathbb{1}(\boldsymbol{\lambda} > \mathbf{0}) \exp \left\{ -\frac{\theta}{2} \boldsymbol{\lambda}' \left[ C^{-1} - \frac{C^{-1} \mathbf{l}' C^{-1}}{\mathbf{l}' C^{-1} \mathbf{l} + \frac{1}{\theta\sigma^2}} \right] \boldsymbol{\lambda} \right\} \\
530 \quad &\approx \mathbb{1}(\boldsymbol{\lambda} > \mathbf{0}) \exp \left\{ -\frac{\theta}{2} \boldsymbol{\lambda}' \tilde{Q} \boldsymbol{\lambda} \right\}
\end{aligned}$$

531 where  $z := \sqrt{\theta \mathbf{l}' C^{-1} \mathbf{l} + \frac{1}{\sigma^2}} \left( y - \frac{\mathbf{l}' C^{-1} \boldsymbol{\lambda}}{\mathbf{l}' C^{-1} \mathbf{l} + \frac{1}{\theta\sigma^2}} \right)$ , and  $\tilde{Q} := C^{-1} - \frac{C^{-1} \mathbf{l}' C^{-1}}{\mathbf{l}' C^{-1} \mathbf{l}}$ .

## 532 [Appendix E. additional experiments results.](#)

533 **E.1. Evaluation metrics.** **Sum of square errors at grid points :** is computed by summing  
534 up squared differences between the median of predicted intensity function values and ground truth  
535 values.

536 **Coverage at grid points :** is the percentage of points at which the true intensity lies within the  
537 corresponding 95% credible intervals.

538 **Credible interval width :** is computed as the average width of the 95% posterior credible  
539 intervals across all grid points.

540 These three statistics are evaluated on a regular grid of 100 points per dataset. We report the  
541 25th, 50th (median), and 75th percentiles of the resulting values across 100 datasets.

542 **E.2. Simulations.** Here, we present additional qualitative and quantitative results for the two  
543 Poisson processes with intensities given in Equations [\(3.1\)](#) and [\(3.2\)](#), as well as posterior sensitivity  
544 to different values of  $\epsilon$ , as shown in [Figure 9](#). In addition to [Figure 1](#), the trace plots and his-  
545 tograms in [Figures 4](#) and [5](#) illustrate traceplots of the latent GP at midpoint and histograms of the  
546 cumulative intensity function for the two simulated datasets with intensities  $\lambda_1(s)$  and  $\lambda_2(s)$ . All  
547 results demonstrate that the MCMC algorithm converges well and modes of histograms approach  
548 the ground truth values for the cumulative intensity function.

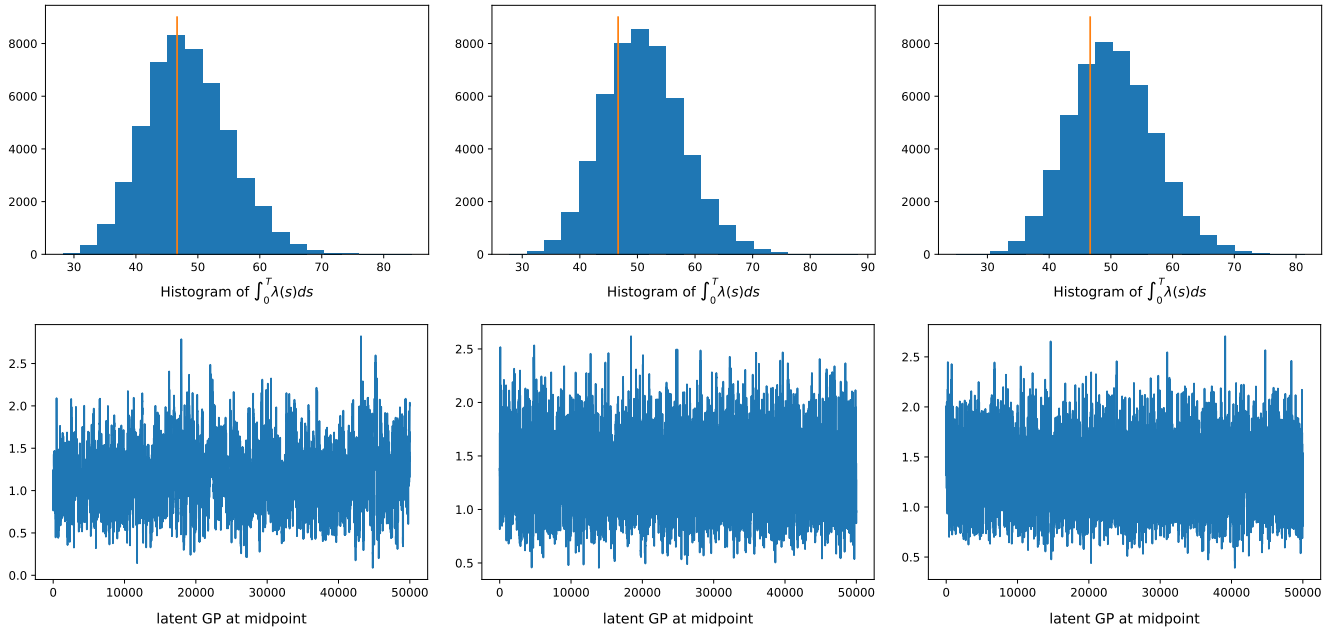


Figure 4: MCMC traceplots for posterior samples of latent GP at midpoint along with histograms of the cumulative intensity function for the same simulated dataset from  $\lambda_1(s)$  as that in top row of Figure 1. On the top row, the red vertical line in each histogram represents the ground truth value for  $\int_0^T \lambda_1(s)ds$ . The three columns from left to right correspond to results using methods RI-BM, RI-MAP and RI-MLE respectively.

549 We also include samples from the truncated Gaussian, log-Gaussian, and sigmoid-Gaussian  
 550 processes in Figure 10. Tables 4 to 7 report quantiles of the same performance evaluation metrics  
 551 as those in Tables 1 and 2, evaluated across 100 simulated datasets from the original, doubled, and  
 552 tripled versions of both intensities. In addition to reporting results at grid points, we also include  
 553 metrics computed at the observed locations.

554 **E.3. Earthquakes in Japan & redwoods.** Figures 6 and 8 mainly present traceplots of la-  
 555 tent GP and histograms of the cumulative intensity function for real examples in Subsections 3.2  
 556 and 3.3. Additionally, posterior results obtained using INLA for Subsection 3.2 are shown in Fig-  
 557 ure 6. Figure 7 displays the posterior results for the mixed data described in Subsection 3.4,  
 558 presented separately from the posterior results for the recurrent data in Subsection 3.2. In Fig-  
 559 ure 8, we also include the posterior median intensity estimated via the kernel smoothing method  
 560 for Subsection 3.3.

561 Table 8 reports the effective sample size at the midpoint, along with the minimum and maximum  
 562 values across all grid points for the earthquake example in Subsection 3.2. Similarly, Table 9 reports  
 563 these metrics for the example in Subsection 3.3.

Expected Event Counts	Methods	SSE at Observations	Coverage at Observations	Credible Interval Width
46.65	RI-BM	<b>3.21 (2.25, 4.16)</b>	98% (95%, 100%)	1.32 (1.25, 1.39)
	SGCP-BM	4.07 (2.86, 7.57)	100% (100%, 100%)	1.60 (1.46, 1.73)
	INLA-BM	4.19 (3.18, 6.32)	100% (100%, 100%)	2.02 (1.69, 2.30)
	RI-MAP	4.23 (3.08, 5.46)	90% (77%, 100%)	0.96 (0.80, 1.18)
	SGCP-MAP	<b>3.63 (3.04, 4.59)</b>	88% (74%, 100%)	0.94 (0.80, 1.11)
	RI-MLE	3.55 (2.40, 4.41)	100% (94%, 100%)	1.19 (1.14, 1.24)
93.3	SGCP-MLE	<b>3.17 (2.08, 4.52)</b>	100% (96%, 100%)	1.15 (1.09, 1.18)
	RI-BM	<b>17.70 (13.72, 23.45)</b>	99% (94%, 100%)	1.83 (1.74, 1.93)
	SGCP-BM	19.42 ( <b>13.21</b> , 33.42)	100% (100%, 100%)	2.58 (2.43, 2.75)
	INLA-BM	21.77 (15.63, 35.66)	100% (100%, 100%)	3.06 (2.83, 3.42)
	RI-MAP	24.20 (17.56, 29.65)	93% (77%, 100%)	1.61 (1.44, 1.79)
	RI-MLE	<b>14.66 (10.76, 25.12)</b>	100% (98%, 100%)	1.81 (1.76, 1.88)
139.95	RI-BM	<b>49.32 (38.53, 63.82)</b>	99% (93%, 100%)	2.32 (2.20, 2.50)
	INLA-BM	65.31 (42.13, 101.72)	100% (99%, 100%)	4.14 (3.77, 4.51)
	RI-MAP	63.46 (35.73, 89.16)	94% (77%, 100%)	2.09 (1.88, 2.34)
	RI-MLE	<b>37.26 (20.94, 66.00)</b>	100% (96%, 100%)	2.35 (2.28, 2.41)
Expected Event Counts	Methods	SSE at 100 Grids	Coverage at 100 Grids	Credible Interval Width at 100 Grids
93.3	RI-BM	<b>16.20 (12.58, 20.97)</b>	99% (96%, 100%)	1.68 (1.57, 1.74)
	SGCP-BM	17.84 (13.54, 28.46)	100% (100%, 100%)	2.14 (2.02, 2.28)
	INLA-BM	19.95 (15.12, 27.41)	100% (99%, 100%)	2.33 (2.21, 2.51)
	RI-MAP	20.60 (15.11, 26.20)	92% (80%, 100%)	1.39 (1.25, 1.55)
	RI-MLE	<b>13.35 (9.95, 19.11)</b>	100% (95%, 100%)	1.55 (1.50, 1.60)
	RI-BM	<b>27.91 (19.76, 37.28)</b>	99% (93%, 100%)	2.07 (1.95, 2.21)
139.95	INLA-BM	35.65 (24.77, 53.81)	100% (99%, 100%)	3.15 (2.91, 3.34)
	RI-MAP	35.86 (18.92, 48.65)	94% (81%, 100%)	1.79 (1.62, 1.94)
	RI-MLE	<b>21.44 (11.74, 37.21)</b>	100% (96%, 100%)	1.98 (1.92, 2.03)

Table 4: Performance comparison on simulations with intensities  $\lambda_1(s)$ ,  $2\lambda_1(s)$  and  $3\lambda_1(s)$ . The last three columns present quantities in the format: 0.50 quantile (0.25 quantile, 0.75 quantile). Bold is the best among methods with the same kernel.

Expected Event Counts	Methods	Average Time $\pm$ Standard Deviation
93.3	RI-BM	$3.68 \pm 1.52$ s
	SGCP-BM	$234392.72 \pm 21852.78$ s
	INLA-BM	$4.81 \pm 0.85$ s
	RI-MAP	$3.67 \pm 0.29$ s
	RI-MLE	$3.81 \pm 0.39$ s
139.95	RI-BM	$3.22 \pm 0.60$ s
	INLA-BM	$4.79 \pm 0.12$ s
	RI-MAP	$3.97 \pm 0.30$ s
	RI-MLE	$4.22 \pm 0.28$ s

Table 5: Running time for estimating intensities  $2\lambda_1(s)$  and  $3\lambda_1(s)$ .

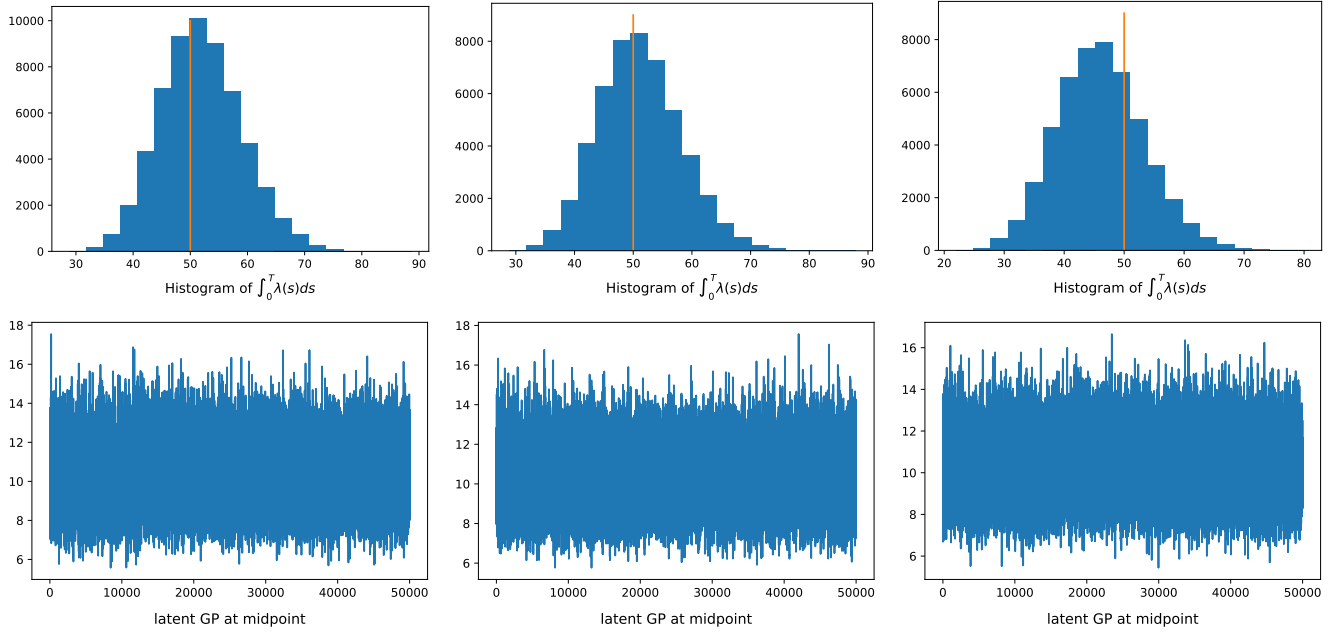


Figure 5: MCMC traceplots for posterior samples of latent GP at midpoint along with histograms of the cumulative intensity function for the same simulated dataset from  $\lambda_2(s)$  as that in bottom row of Figure 1. On the top row, the red vertical line in each histogram represents the ground truth value for  $\int_0^T \lambda_2(s)ds$ . The three columns from left to right correspond to results using methods RI-BM, RI-MAP and RI-MLE respectively.

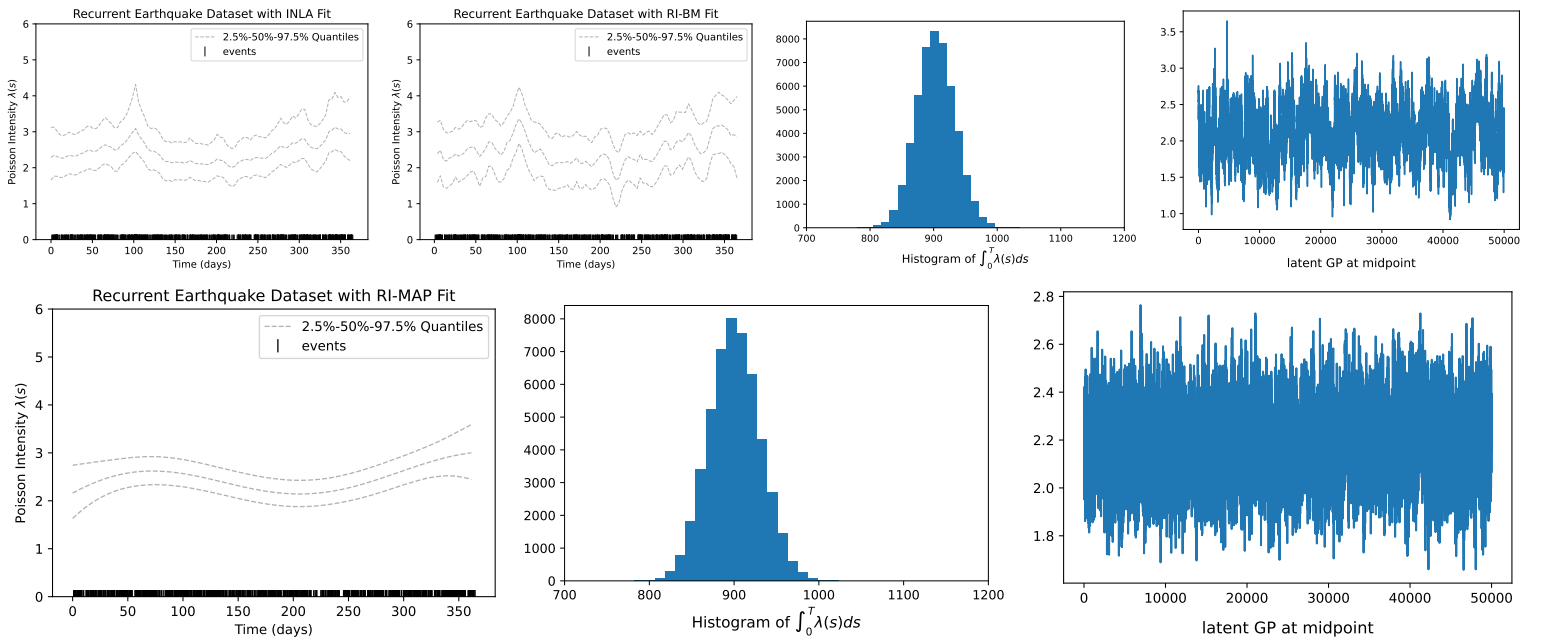


Figure 6: MCMC traceplots for posterior samples of latent GP at midpoint along with histograms of the cumulative intensity function for the recurrent earthquake data in Subsection 3.2. The panel in the top-left corner presents the posterior results using INLA-BM. The remaining panels in the top row show results obtained using our proposed method, RI-BM. The bottom row displays results from our alternative approach, RI-MAP.

Expected Event Counts	Methods	SSE at Observations	Coverage at Observations	Credible Interval Width
50	RI-BM SGCP-BM INLA-BM	<b>40.57 (11.68, 107.33)</b> 112.96 (55.14,236.44) 146.70 (86.12,251.31)	100% (100%,100%) 100% (100%,100%) 100% (100%,100%)	6.28 (5.95,6.73) 9.10 (8.45,10.08) 12.71 (11.79,14.13)
	RI-MAP SGCP-MAP	63.88 ( <b>18.20,152.75</b> ) 65.93 (18.21,213.01)	100% (100%,100%) 100% (100%,100%)	5.60 (5.26,5.87) 5.82 (5.43,6.29)
	RI-MLE SGCP-MLE	<b>43.51 (13.69,133.90)</b> 53.96 (17.70,136.95)	100% (100%,100%) 100% (100%,100%)	5.84 (5.41,6.84) 5.65 (5.29,5.95)
100	RI-BM SGCP-BM INLA-BM	<b>282.11 (72.87,585.80)</b> 778.82 (267.56,1.65e+3) 801.15 (450.33,1.40e+3)	100% (100%,100%) 100% (100%,100%) 100% (100%,100%)	9.10 (8.52,9.77) 14.72 (13.37,16.01) 18.92 (18.03,20.66)
	RI-MAP RI-MLE	<b>213.48</b> (82.61,693.65) 677.97 (143.01,4.38e+3)	100% (100%,100%) 100% (100%,100%)	7.75 (7.46,8.16) 8.15 (7.51,36.28)
150	RI-BM INLA-BM	<b>1.19e+3 (205.51, 2.44e+3)</b> 2.16e+3 (1.30e+3,3.70e+3)	100% (100%,100%) 100% (100%,100%)	12.06 (11.11,13.60) 24.53 (23.13,26.05)
	RI-MAP RI-MLE	<b>605.16</b> (218.68,1.52e+3) 4.21e+5 (1.36e+5,2.62e+6)	100% (100%,100%) 0% (0%,48%)	9.42 (9.20,9.85) 36.90 (16.19,110.35)
Expected Event Counts	Methods	SSE at 100 Grids	Coverage at 100 Grids	Credible Interval Width at 100 Grids
100	RI-BM SGCP-BM INLA-BM	<b>298.82 (75.56,571.92)</b> 884.86 (303.59,1.47e+3) 850.71 (512.17,1.48e+3)	100% (100%,100%) 100% (100%,100%) 100% (100%,100%)	9.05 (8.49,9.73) 14.94 (13.60,16.19) 18.15 (17.43,19.73)
	RI-MAP RI-MLE	<b>213.53</b> (79.55,675.76) 396.97 (131.65,1.49e+3)	100% (100%,100%) 100% (100%,100%)	7.75 (7.46,8.16) 8.15 (7.51,37.86)
150	RI-BM INLA-BM	<b>830.65 (138.58,1.74e+3)</b> 1.61e+3 (947.39,2.61e+3)	100% (100%,100%) 100% (100%,100%)	12.04 (11.09,13.52) 23.59 (22.42,24.99)
	RI-MAP RI-MLE	<b>434.85</b> (151.44,999.74) 1.94e+5 (6.97e+4,1.69e+6)	100% (100%,100%) 0% (0%,96%)	9.42 (9.20,9.85) 36.90 (16.24,117.17)

Table 6: Performance comparison on simulations with intensities  $\lambda_2(s)$ ,  $2\lambda_2(s)$  and  $3\lambda_2(s)$ . The last three columns present quantities in the format: 0.50 quantile (0.25 quantile, 0.75 quantile). Bold is the best among methods with the same kernel.

Expected Event Counts	Methods	Average Time $\pm$ Standard Deviation
100	RI-BM SGCP-BM INLA-BM	1.83 $\pm$ 0.36 s 43811.94 $\pm$ 9316.78 s 4.47 $\pm$ 0.20 s
	RI-MAP	3.02 $\pm$ 0.24 s
	RI-MLE	3.82 $\pm$ 0.54 s
150	RI-BM INLA-BM	2.45 $\pm$ 0.89 s 4.34 $\pm$ 0.07 s
	RI-MAP	3.27 $\pm$ 0.18 s
	RI-MLE	5.28 $\pm$ 0.61 s

Table 7: Running time for estimating intensities  $2\lambda_2(s)$  and  $3\lambda_2(s)$ .

Table 8: Effective sample size per 10000 iterations for the recurrent earthquake data in Subsection 3.2.

Methods	Minimum ESS	Maximum ESS	ESS at midpoint
RI-MAP	123.31	621.00	218.79
RI-BM	13.80	52.87	35.28

Table 9: Effective sample size per 10000 iterations for thinned chains in Subsection 3.3.

Methods	Minimum ESS	Maximum ESS	ESS at midpoint
RI-MAP	59.99	376.55	155.54
RI-BM	5.88	148.57	86.52

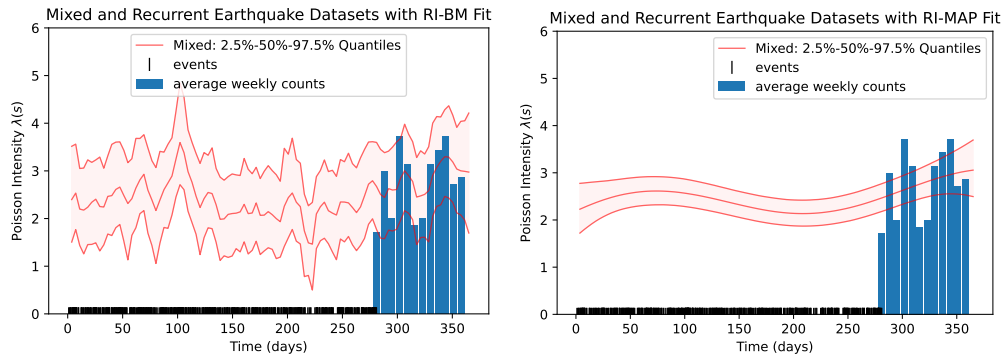


Figure 7: 2.5%–50%–97.5% posterior quantiles of the intensity function for mixed earthquake data in Subsection 3.4. Left panel corresponds to results using a Brownian motion covariance kernel and the right panel corresponds to results using a squared exponential kernel with MAP.

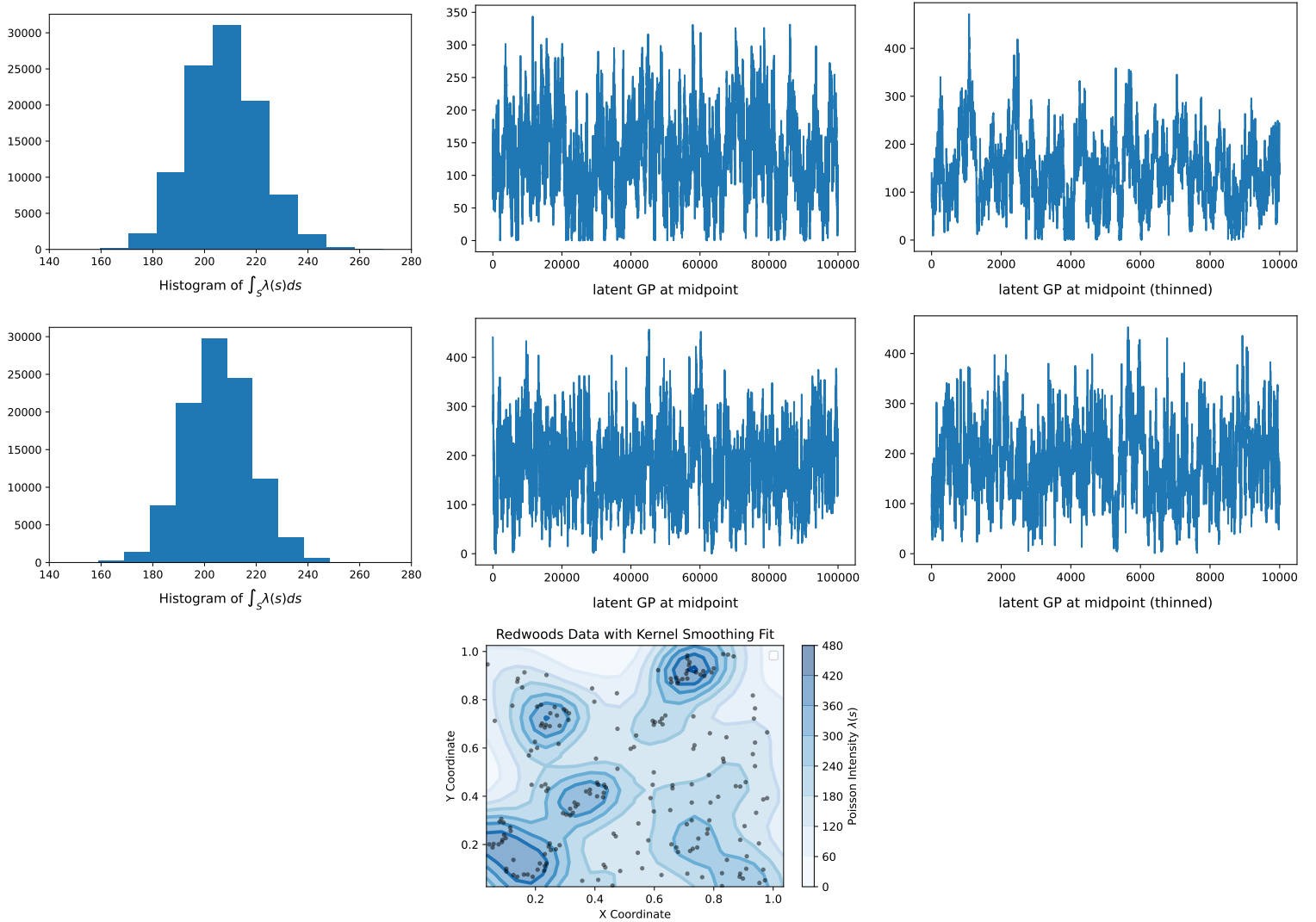


Figure 8: MCMC traceplots for posterior samples of latent GP at midpoint along with histograms of the cumulative intensity function for the redwoods data in Subsection 3.3. The top row presents results obtained using our proposed method, RI-BM, while the middle row corresponds to results from RI-MAP. The bottom row shows the posterior median of the intensity function estimated via kernel smoothing, using a bandwidth of 0.08.

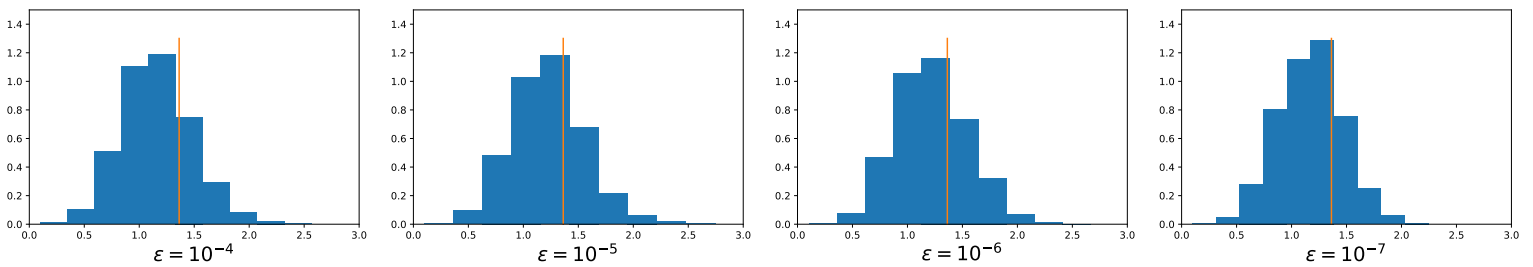
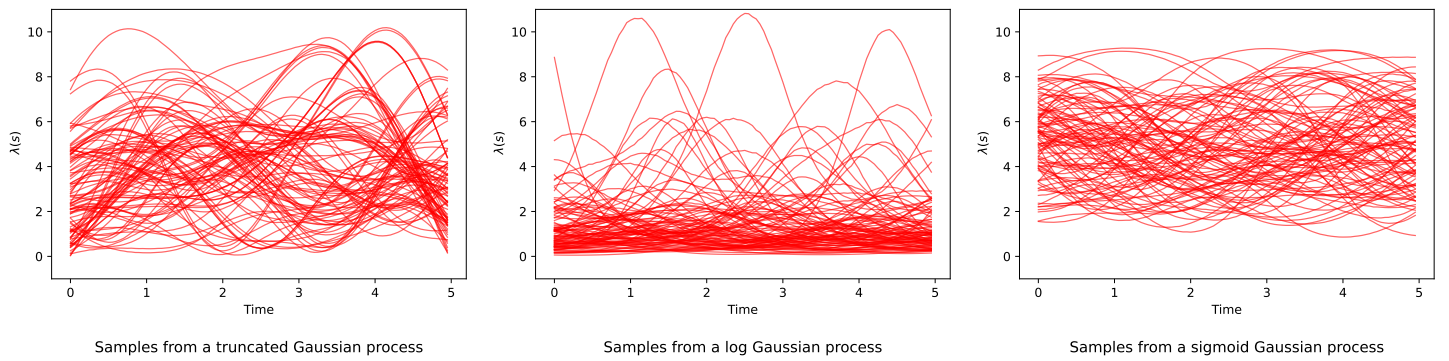


Figure 9: Histograms of posterior samples of latent GP at midpoint for a simulated dataset from  $\lambda_1(s)$  when  $\epsilon = 10^{-4}, 10^{-5}, 10^{-6}, 10^{-7}$  (from left to right).



Samples from a truncated Gaussian process

Samples from a log Gaussian process

Samples from a sigmoid Gaussian process

Figure 10: Left: samples from a squared-exponential covariance truncated GP with  $\theta_0 = 10$  and  $\theta_1 = 1$ ; Middle: samples from a squared-exponential covariance log GP with  $\theta_0 = 0.7$  and  $\theta_1 = 1$ ; Right: samples from a squared-exponential covariance sigmoid GP with  $\theta_0 = 0.7$ ,  $\theta_1 = 1$  and  $\lambda_{sup} = 10$ .

## REFERENCES

- [1] I. S. ABRAMSON, *On bandwidth variation in kernel estimates-a square root law*, The annals of Statistics, (1982), pp. 1217–1223.
- [2] R. P. ADAMS, I. MURRAY, AND D. J. MACKAY, *Tractable nonparametric Bayesian inference in Poisson processes with Gaussian process intensities*, in Proceedings of the 26th Annual International Conference on Machine Learning, 2009, pp. 9–16.
- [3] V. AGLIETTI, E. V. BONILLA, T. DAMOULAS, AND S. CRIPPS, *Structured variational inference in continuous Cox process models*, Advances in Neural Information Processing Systems, 32 (2019).
- [4] A. BADDELEY, E. RUBAK, AND R. TURNER, *Spatial point patterns: methodology and applications with R*, CRC press, 2015.
- [5] A. BADDELEY AND R. TURNER, *Spatstat: an r package for analyzing spatial point patterns*, Journal of statistical software, 12 (2005), pp. 1–42.
- [6] J. E. BARRETT AND A. C. COOLEN, *Gaussian process regression for survival data with competing risks*, arXiv preprint arXiv:1312.1591, (2013).
- [7] R. BARTOSZYŃSKI, B. W. BROWN, C. M. MCBRIDE, AND J. R. THOMPSON, *Some nonparametric techniques for estimating the intensity function of a cancer related nonstationary poisson process*, The Annals of Statistics, (1981), pp. 1050–1060.
- [8] M. BERMAN AND P. DIGGLE, *Estimating weighted integrals of the second-order intensity of a spatial point process*, Journal of the Royal Statistical Society Series B: Statistical Methodology, 51 (1989), pp. 81–92.
- [9] R. T. CHEN, B. AMOS, AND M. NICKEL, *Neural spatio-temporal point processes*, arXiv preprint arXiv:2011.04583, (2020).
- [10] S. CHEN, J. Y. S. XI, AND W. K. V. CHAN, *Estimating spline-based nonhomogeneous poisson intensities using constrained quadratic programming*, in 2023 Winter Simulation Conference (WSC), IEEE, 2023, pp. 339–350.
- [11] D. R. COX, *Some statistical methods connected with series of events*, Journal of the Royal Statistical Society: Series B (Methodological), 17 (1955), pp. 129–157.
- [12] T. M. DAVIES AND A. BADDELEY, *Fast computation of spatially adaptive kernel estimates*, Statistics and Computing, 28 (2018), pp. 937–956.
- [13] T. M. DAVIES, J. C. MARSHALL, AND M. L. HAZELTON, *Tutorial on kernel estimation of continuous spatial and spatiotemporal relative risk*, Statistics in medicine, 37 (2018), pp. 1191–1221.
- [14] P. DIGGLE, *A kernel method for smoothing point process data*, Journal of the Royal Statistical Society: Series C (Applied Statistics), 34 (1985), pp. 138–147.
- [15] P. J. DIGGLE, P. MORAGA, B. ROWLINGSON, AND B. M. TAYLOR, *Spatial and spatio-temporal log-Gaussian Cox processes: extending the geostatistical paradigm*, (2013).
- [16] C. DONNER AND M. OPPER, *Efficient Bayesian inference of sigmoidal Gaussian Cox processes*, Journal of Machine Learning Research, 19 (2018), pp. 1–34.
- [17] D. DUVENAUD, *Automatic model construction with Gaussian processes*, PhD thesis, 2014.
- [18] T. FERNÁNDEZ, N. RIVERA, AND Y. W. TEH, *Gaussian processes for survival analysis*, Advances in Neural Information Processing Systems, 29 (2016).
- [19] S. FLAXMAN, Y. W. TEH, AND D. SEJDINOVIC, *Poisson intensity estimation with reproducing kernels*, in Artificial Intelligence and Statistics, PMLR, 2017, pp. 270–279.
- [20] P. GUTTORP AND T. L. THORARINSDOTTIR, *What happened to discrete chaos, the Quenouille process, and the sharp Markov property? some history of stochastic point processes*, International Statistical Review, 80 (2012), pp. 253–268.
- [21] P. HENNIG, M. A. OSBORNE, AND H. P. KERSTING, *Probabilistic numerics: computation as machine learning*, Cambridge University Press, 2022.
- [22] J. F. C. KINGMAN, *Poisson processes*, vol. 3, Clarendon Press, 1992.
- [23] A. KOTTAS, *Dirichlet process mixtures of Beta distributions, with applications to density and intensity estimation*, in Workshop on Learning with Nonparametric Bayesian Methods, 23rd International Conference on Machine Learning (ICML), vol. 47, Citeseer, 2006.
- [24] A. KOTTAS AND B. SANSÓ, *Bayesian mixture modeling for spatial Poisson process intensities, with applications to extreme value analysis*, Journal of Statistical Planning and Inference, 137 (2007), pp. 3151–3163.
- [25] T. LAWRENCE, A. BADDELEY, R. K. MILNE, AND G. NAIR, *Point pattern analysis on a region of a sphere*, Stat, 5 (2016), pp. 144–157.
- [26] M. LEGG AND M. CHITRE, *Clustering of snapping shrimp snaps on long time scales: a simulation study*, Acoustics 2012, Fremantle, Australia, (2012).
- [27] P. W. LEWIS AND G. S. SHEDLER, *Simulation of nonhomogeneous Poisson processes by thinning*, Naval Research Logistics Quarterly, 26 (1979), pp. 403–413.
- [28] C. LLOYD, T. GUNTER, M. OSBORNE, AND S. ROBERTS, *Variational inference for Gaussian process modulated Poisson processes*, in International Conference on Machine Learning, PMLR, 2015, pp. 1814–1822.
- [29] A. F. LÓPEZ-LOPERA, S. JOHN, AND N. DURRANDE, *Gaussian process modulated Cox processes under linear inequality constraints*, in The 22nd International Conference on Artificial Intelligence and Statistics, PMLR,

- 625 2019, pp. 1997–2006.

626 [30] S. MARTINO, R. AKERKAR, AND H. RUE, *Approximate Bayesian inference for survival models*, Scandinavian  
627 Journal of Statistics, 38 (2011), pp. 514–528.

628 [31] J. MØLLER, A. N. PETTITT, R. REEVES, AND K. K. BERTHELSEN, *An efficient Markov Chain Monte Carlo  
629 method for distributions with intractable normalising constants*, Biometrika, 93 (2006), pp. 451–458.

630 [32] J. MØLLER, A. R. SYVERSVEEN, AND R. P. WAAGEPETERSEN, *Log Gaussian Cox processes*, Scandinavian  
631 Journal of Statistics, 25 (1998), pp. 451–482.

632 [33] L. E. MORGAN, B. L. NELSON, A. C. TITMAN, AND D. J. WORTHINGTON, *A spline-based method for modelling  
633 and generating a nonhomogeneous poisson process*, in 2019 Winter Simulation Conference (WSC), IEEE,  
634 2019, pp. 356–367.

635 [34] P. MÖRTERS AND Y. PERES, *Brownian motion*, vol. 30, Cambridge University Press, 2010.

636 [35] K. MULLEN, D. ARDIA, D. L. GIL, D. WINDOVER, AND J. CLINE, *DEoptim: An R package for global  
637 optimization by differential evolution*, Journal of Statistical Software, 40 (2011), pp. 1–26.

638 [36] I. MURRAY, R. ADAMS, AND D. MACKAY, *Elliptical slice sampling*, in Proceedings of the thirteenth Interna-  
639 tional Conference on Artificial Intelligence and Statistics, JMLR Workshop and Conference Proceedings,  
640 2010, pp. 541–548.

641 [37] I. MURRAY, Z. GHAHRAMANI, AND D. MACKAY, *MCMC for doubly-intractable distributions*, arXiv preprint  
642 arXiv:1206.6848, (2012).

643 [38] R. PYKE, *Partial sums of matrix arrays, and Brownian sheets*, Stochastic Analysis, (1973), pp. 331–348.

644 [39] J. QUINONERO-CANDELA AND C. E. RASMUSSEN, *A unifying view of sparse approximate Gaussian process  
645 regression*, The Journal of Machine Learning Research, 6 (2005), pp. 1939–1959.

646 [40] H. RAMLAU-HANSEN, *Smoothing counting process intensities by means of kernel functions*, The Annals of  
647 Statistics, (1983), pp. 453–466.

648 [41] S. L. RATHBUN AND N. CRESSIE, *Asymptotic properties of estimators for the parameters of spatial inhomoge-  
649 neous Poisson point processes*, Advances in Applied Probability, 26 (1994), pp. 122–154.

650 [42] H. RUE AND L. HELD, *Gaussian Markov random fields: theory and applications*, CRC press, 2005.

651 [43] H. RUE, S. MARTINO, AND N. CHOPIN, *Approximate Bayesian inference for latent Gaussian models by using in-  
652 tegrated nested Laplace approximations*, Journal of the Royal Statistical Society: Series B (Methodological),  
653 71 (2009), pp. 319–392.

654 [44] Y.-L. K. SAMO AND S. ROBERTS, *Scalable nonparametric Bayesian inference on point processes with Gaussian  
655 processes*, in International Conference on Machine Learning, PMLR, 2015, pp. 2227–2236.

656 [45] S. SÄRKÄ, *Linear operators and stochastic partial differential equations in Gaussian process regression*, in  
657 Artificial Neural Networks and Machine Learning—ICANN 2011: 21st International Conference on Artificial  
658 Neural Networks, Espoo, Finland, June 14–17, 2011, Proceedings, Part II 21, Springer, 2011, pp. 151–158.

659 [46] D. J. STRAUSS, *A model for clustering*, Biometrika, 62 (1975), pp. 467–475.

660 [47] B. M. TAYLOR, T. M. DAVIES, B. S. ROWLINGSON, AND P. J. DIGGLE, *lgcp: an R package for inference with  
661 spatial and spatio-temporal log-Gaussian Cox processes*, Journal of Statistical Software, 52 (2013), pp. 1–40.

662 [48] B. M. TAYLOR, T. M. DAVIES, B. S. ROWLINGSON, AND P. J. DIGGLE, *Bayesian inference and data aug-  
663 mentation schemes for spatial, spatiotemporal and multivariate log-Gaussian Cox processes in R*, Journal of  
664 Statistical Software, 63 (2015), pp. 1–48.

665 [49] B. M. TAYLOR AND P. J. DIGGLE, *INLA or MCMC? A tutorial and comparative evaluation for spatial prediction  
666 in log-Gaussian Cox processes*, Journal of Statistical Computation and Simulation, 84 (2014), pp. 2266–2284.

667 [50] Y. TEH AND V. RAO, *Gaussian process modulated renewal processes*, Advances in Neural Information Processing  
668 Systems, 24 (2011).

669 [51] M. TENG, F. NATHOO, AND T. D. JOHNSON, *Bayesian computation for Log-Gaussian Cox processes: A com-  
670 parative analysis of methods*, Journal of statistical computation and simulation, 87 (2017), pp. 2227–2252.

671 [52] S. I. WATSON, *Twenty ways to estimate the Log Gaussian Cox Process model with point and aggregated case  
672 data: the rts2 package for R*, arXiv preprint arXiv:2403.09448, (2024).

673 [53] C. K. WILLIAMS AND C. E. RASMUSSEN, *Gaussian processes for machine learning*, vol. 2, MIT press Cambridge,  
674 MA, 2006.

675 [54] N. YANNAROS, *Weibull renewal processes*, Annals of the Institute of Statistical Mathematics, 46 (1994), pp. 641–  
676 648.